Masteroppgave

NTNU
Norges teknisk-naturvitenskapelige universitet
Fakultet for ingeniørvitenskap
Institutt for konstruksjonsteknikk

Ingeborg Wilsher

Modelling of fluid structure interaction using artificial neural networks for running fracture problems in steel pipes

Masteroppgave i Ingeniørvitenskap og IKT
Veileder: David Morin
Juli 2023

NTNU
Kunnskap for en bedre verden

Ingeborg Wilsher

Modelling of fluid structure interaction using artificial neural networks for running fracture problems in steel pipes

Masteroppgave i Ingeniørvitenskap og IKT
Veileder: David Morin
Juli 2023

Norges teknisk-naturvitenskapelige universitet
Fakultet for ingeniørvitenskap
Institutt for konstruksjonsteknikk

NTNU
Kunnskap for en bedre verden

Department of Structural Engineering
Faculty of Engineering
NTNU- Norwegian University of Science and Technology

ACCESSIBILITY

MASTER THESIS 2023

SUBJECT AREA: Computational mechanics	DATE: 03.07.2023	NO. OF PAGES: 20+50+15

TITLE:

Modelling of fluid structure interaction using artificial neural networks for running fracture problems in steel pipes

Modellering av fluid struktur interaksjon ved nevrale nettverk for løpende brudd i rørledninger

BY:

Ingeborg Wilsher

SUMMARY:
Carbon dioxide capture and storage have become important actions for reducing the greenhouse gas emissions in the atmosphere. For full scale carbon capture and storage to be successful and implemented in a global scale, safe and reliable transportation and infrastructure are required. The Battelle Two-curve method has previously been the dominant approach for assessing fracture propagation control in pipelines, but has shown to give non-conservative results. Other approaches can be time-consuming and with high computational cost. Due to this, investigation on incorporating machine learning models in engineering tools for efficient simulations have been done. Research has shown that the crack propagating force of a running ductile fracture has a strong spatial variation in two directions. In the thesis, the development of a reference pressure decay model for the pressure inside the pipe during the event of a running ductile fracture has been presented. The developed model will account for the spatial variations and the depressurisation of CO2. The pressure model developed was used as loading for simulation of running ductile fracture in a FEM-program. Four pipelines were simulated and the results from the simulations were evaluated. Further, machine learning model were implemented, and trained using data obtained from the simulations. Data from three different pipeline simulations was used for testing the developed machine learning model, and assessing the predictive capabilities. From the testing, it was found that the trained machine learning models were able to predict pressure in a pipe with smaller diameter and longer propagating crack. For a larger pipe diameter the models were not able to predict all aspects of the pressure curves. To overcome this, the models need to be trained with more diverse data, containing multiple pipe diameters. From the work, it is believed that a machine learning model can be implemented in engineering tools for efficient simulations of running ductile fractures.

RESPONSIBLE TEACHER: Prof. David Morin

SUPERVISOR(S): Prof. David Morin

CARRIED OUT AT: SIMLab, The department of Structural Engineering, NTNU

Department of Structural Engineering
FACULTY OF ENGINEERING SCIENCE
NTNU – Norwegian University of Science and Technology

MASTER'S THESIS 2023

for

Ingeborg Wilsher

Modelling of fluid structure interaction using artificial neural networks for running fracture problems in steel pipes

CO_2 capture and storage relies on a safe system to transport gas through pipelines. These pipelines can be subjected to accident loads which can initiate fracture. Due to the internal pressure of the pipelines, running fracture can thus occur and its impact should be evaluated by means of numerical simulations. In previous works, running cracks in pressurized pipelines was investigated from a material point of view and a procedure valid within an engineering context was established. In this procedure, the pressure applied onto the pipeline was idealized and potential fluid-structure interaction (FSI) problems were neglected. To account for potential FSI effects, advanced numerical simulations are usually required. Either smooth particle hydrodynamics or computational fluid dynamics simulations are rather common numerical methods to simulate such problems. While these methods can provide high accuracy, they also come at heavy computational costs which renders them incompatible within engineering practices.

The main idea behind this project is to evaluate how machine learning, and artificial neural networks, can be used to incorporate FSI effects within an engineering tool for simulating running cracks in pipelines. In other words, we want to replace complex fluid-structure analyses by a surrogate model for efficient simulations.

The main tasks of the research project are as follows:

1. Literature review: To perform a literature review on experiments and modelling of running ductile fracture in steel pipes with a focus on the representation of the fluid pressure.
2. Numerical study: To develop a reference pressure decay model for the fluid pressure behind the crack tip
3. Running fracture: To use the developed pressure decay model in simulations of running fracture in pipelines
4. Machine learning: To develop an artificial neural network capable of representing the applied pressure in pipelines, and assess its predictive capability.
5. Reporting: To report the research work.

Supervisors: David Morin

The thesis must be written according to current requirements and submitted to the Department of Structural Engineering, NTNU, no later than July 3rd, 2023.

NTNU, February 3rd, 2023.

David Morin
Associate Professor

Preface

This master thesis is the concluding part of our Master of Science in Engineering and ICT with a degree specialization in ICT and Structural engineering at the Norwegian University of Science and Technology (NTNU). I would like to thank my academic supervisor David Morin for the guidance, resources and feedback I have received throughout this thesis.

Trondheim, June 2023

Summary

Carbon dioxide capture and storage have become important actions for reducing the greenhouse gas emissions in the atmosphere. For full scale carbon capture and storage to be successful and implemented in a global scale, safe and reliable transportation and infrastructure are required. The Battelle Two-curve method has previously been the dominant approach for assessing fracture propagation control in pipelines, but has shown to give non-conservative results. Other approaches can be time-consuming and with high computational cost. Due to this, investigation on incorporating machine learning models in engineering tools for efficient simulations have been done. Research has shown that the crack propagating force of a running ductile fracture has a strong spatial variation in two directions. In the thesis, the development of a reference pressure decay model for the pressure inside the pipe during the event of a running ductile fracture has been presented. The developed model will account for the spatial variations and the depressurisation of CO2. The pressure model developed was used as loading for simulation of running ductile fracture in a FEM-program. Four pipelines were simulated and the results from the simulations were evaluated. Further, machine learning model were implemented, and trained using data obtained from the simulations. Data from three different pipeline simulations was used for testing the developed machine learning model, and assessing the predictive capabilities. From the testing, it was found that the trained machine learning models were able to predict pressure in a pipe with smaller diameter and longer propagating crack. For a larger pipe diameter the models were not able to predict all aspects of the pressure curves. To overcome this, the models need to be trained with more diverse data, containing multiple pipe diameters. From the work, it is believed that a machine learning model can be implemented in engineering tools for efficient simulations of running ductile fractures.

Sammendrag

Karbonfangts og lagring har blitt et viktig tiltak for å redusere klimagassutslippene i atmorsfæren. For at karbonfangst og lagring skal være vellykket i fullskala, kreves det trygg og pålitelig transport og infrastruktur. Tidligere har metoden "Battelle two-curve method" vært den dominerende metoden brukt for å dimensjonere rør med kontroll av sprekkdannelsene. Metoden har vist seg å gi ikke-konservative resultater for CO_2. Andre metoder kan være tidkrevenede, og kostnadskrevende beregninger. Det er derfor ønskelig å undersøke muligheten for å implementere en maskinlæringsmodell i ingeniørverktøy for mer effektive simuleringer. Forskning har vist at kreftene som virker på et løpende duktilt brudd har en romslig variasjon i to retninger. I denne oppgaven er det presentert en trykkmodell som tar hensyn til disse romslige variasjonene. Videre har trykkavlastningen av CO_2 blitt tatt i betraktning for å kunne beskrive alle mekanismene for trykket i røret. Den utviklede trykkmodellen ble brukt som last for simulering av duktile brudd i et FEM-program. Fire rørledninger med varierende geometri ble simulert, og resultatene ble evaluert. Videre ble maskinlæringsmodeller implementert, og trent på data fra en av simuleringene av rørledning. Maskinlæringsmodellen ble testet på data fra tre andre simuleringer. Resultatene fra testingen indikerte at maskinlæringsmodellene kan med relativ høy nøyaktighet predikere trykket i et rør med mindre diameter og lenger sprekkdannelse. For rør med større diameter vil ikke modellene prestere like godt. For å takle dette må maskinlæringsmodellene trenes med flere diametere på rør. Basert på arbeidet er det anslått at en maskinlæringsmodell kan implementeres i ingeniørverktøy for effektive simuleringer av løpende duktile brudd.

List of Abbreviations

AI	Artificial intelligence
ANN	Artificial Neural networks
CCS	Carbon capture and storage
CFD	Computational Fluid Dynamics
CO_2	Carbon dioxide
CTOA	Crack tip opening angle
CVN	Charpy V-notch
FEM	Finite Element method
FFNN	Feedforward Neural networks
FPC	Fracture propagation control
FSI	Fluid-structure interaction
GTN	Gurson-Tvergaard-Needlemant
HEM	Homogenous equilibrium model
LCO_2	Liquid CO_2
MSE	Mean squared error
OD	Outer diameter
RDF	Running ductile fracture
SPH	Smoothed particle hydrodynamics
TCM	Two-curve methods

Symbols

A	Area
d	Diameter
OD	Outer diameter
E	Youngs modulus
l_{crack}	Crack length
l_{pipe}	Pipe length
l_{ref}	Reference pressure decay length
p_a	Arrest pressure
p_i	Initial pressure
p_{sat}	Saturation pressure
p	Pressure
R	Pipe radius
V_{crack}	Crack speed
V_w	Decompression speed
w_{crack}	Crack width
x	Axial position
Z_c	Position of crack during simulation
Z	Distance to crack tip

Contents

Chapter 1

Introduction

1.1 Research context

In an effort to reduce the world's greenhouse gasses and combat climate change, the capture and storage of carbon dioxide (CO_2) have become important and necessary actions. The purpose of carbon dioxide capture and storage (CCS) is to limit the CO_2 emission in the atmosphere by capturing, transporting and storing CO_2[1]. According to the International Energy Agency, CCS can contribute to a reduction in CO_2 emissions with approximately 6 Gt per year in 2050 [2]. The process of CCS consists of three parts: capture, transport, and storage of CO_2. The CO_2 can be captured from waste gases at power plants and industrial production sites[3]. According to Norwegian Petroleum, geological storage under the seabed is regarded as one of the most secure options for permanent storage in Norwegian CCS projects[4]. In order to inject the captured CO_2 under the seabed, the CO_2 is pressurized into liquid CO_2 (LCO_2) and transported by pipelines from an onshore terminal to the seabed. For CCS to be successful, preventing leakage during transportation and storage is vital, and design of a safe and reliable CO2-transport system is necessary[5].

If a pressurized pipeline is subject to an initial fracture, the rupture can either end in an immediate arrest or evolve into a running ductile fracture (RDF) [6]. A running ductile fracture is a fracture mode experienced in high-pressure gas pipelines, where a crack propagates along the pipe for a large distance [7, 8]. Previous studies have shown that pipelines transporting CO_2 are more prone to RDF, compared to pipelines with natural gas [9, 10]. This is mainly due to the high operating pressures of LCO_2, as well as the phase shift CO_2 will go through. To prevent a running ductile fracture, actions like increased thickness, selection of stronger material, or the use of crack arrestors can be used for design[5]. However, these actions all increase the cost of CCS projects. It is of interest to design pipelines ensuring the integrity of the structure withouth increased costs. The Battelle two-curve method has previously been a commonly used tool for design of pipelines[11]. However, experimental tests and research have found the two-curve method as non-conservative[12]. Due to this, further research and methods for describing an RDF phenomenon in CCS are needed. When designing for fracture propagation control in pipelines, an important component is the fluid pressure inside the pipe. The crack driving force of an RDF stems from the pressure from the fluid at the crack tip, and the

pressure distribution behind the crack. Considering that there are no direct methods for calculating this distribution, new methods for modelling the pressure profile at the crack tip and area behind the crack are needed[13, 14].

Artificial intelligence and data-driven approaches have proved to be efficient tools for computing complex non-linear relations. In the last two decades, AI techniques have been developed and applied to solve engineering problems[15]. Within the field of fracture mechanics, the use of AI has had an increasing interest, due to the increasing complexity of numerical material models[16]. The implementation of AI tools can simplify complex damage simulations and can reduce computational costs [15]. If implemented correctly, AI tools could provide become an aid for quickly simulating fracture propagation in pipelines.

1.2 Thesis objective

The objective of this thesis is to investigate different numerical models for pressure from the CO_2 in the pipeline, and how the pressure is related to the crack propagation. A fluid dynamical pressure model should be developed from existing models and evaluated against experimental values. Further, an evaluation of how machine learning, and artificial neural networks, can be implemented for predicting presure during RDF.

The main idea behind this project is to evaluate how machine learning and artificial neural networks can be used to incorporate interacting fluid-structure effects within an engineering tool for simulating running cracks in pipelines. In other words, evaluate the possibility of replacing complex fluid-structure analyses with a surrogate model for efficient simulations.

The objective can be defined as:

1. To develop a reference pressure decay model for the pressure inside the pipe during the event of a running ductile fracture
2. To simulate a running ductile fracture in a pipeline using the developed reference pressure decay model, and evaluate the results from the simulations
3. To develop an artificial neural network capable of predicting the applied pressure in pipelines during RDF, and assess its predictive capabilities

1.3 Scope

The following is the scope of the work:

- Existing experimental test will be used for the development of a reference pressure decay model
- The work will be based on previous findings by Burchardt and Saether[17]
- Surrounding soil and backfill is outside the scope of this thesis.
- The calculations and modelling done will only account for the axial propagation of the crack, not accounting for any deviation such as potential ring-offs.

1.4 Outline of Thesis

Chapter 2 presents the background of running ductile fracture in pipelines as well as design methods for crack propagation control in pipelines.

Chapter 3 presents existing pressure models for the pressure decay of CO_2 in pipelines. Additionally, the development of the reference pressure decay model is described. The reference pressure decay model was based on values obtained through simulations and experiments from the work by Aursand et al. [5].

In chapter 4, the modelling of a pipe simulations of an RDF will be explained. The simulations will lay the foundation for the data used for the training and validation of a machine learning model.

In chapter 5 background of machine learning and previous work will be presented. Furthermore, the implementation of the neural network is presented and predictions for data set belonging to other pipes are analysed.

Chapter 6 contains the concluding remarks of the work presented. Recommendations for possible further work and studies are suggested.

Chapter 2

Running ductilfe fractures in pipelines

This section covers the relevant theory and background on running ductile fractures in pipelines. In order to obtain fracture propagation control in pipelines, the Battelle two-curve method has been the dominant used method previously [18]. New approaches for obtaining fracture propagation have been suggested in the last decade[5, 11]. Background and theory regarding methods for obtaining fracture propagation control in pipelines.

2.1 Formation of RDF

If a pressurized pipeline sustains a small local rupture, caused by either a corrosion damage or third-party damage severe enough, the rupture can either self-arrest or evolve into a running ductile fracture[19]. When considering if such rupture evolves into a running ductile fracture, mainly two factors are considered: the decompression speed of the fluid and the speed of the propagating fracture of the pipeline. If a sudden opening in the pipeline has occurred, the fluid will escape from the opening and two depressurization waves will propagate in each direction from the crack tip openings[12]. The pressure waves have a speed equal to the difference between the local fluid speed and the local speed of sound[9]. The speed of the propagating fracture is controlled by the distributed pressure on the pipe at the opening. These two couples together to determine the arrestability in the pipeline[6]. If the fluid has a high decompression speed, the pressure at the crack tip will drop and the crack will arrest shortly. However, if the fluid has a low decompression speed, the pressure at the crack tip will remain sufficiently high to create a long-running fracture[3].

Several design requirements and guidelines have been created for pressurized pipelines in order to obtain fracture propagation control[20]. The challenge lies in determining the applicability of existing industry standards for natural gasses to CO_2 transportation systems[3]. CO_2 and rich natural gasses have shown to be more prone to running ductile fracture, due to the depressurization of CO_2[10, 12]. An RDF is governed by the interaction between the decompression wave of the fluid and the crack propagation speed. In

pressurized pipelines carrying liquid-phase fluids, such as water or oil, the fluids will have the same state both before and after the decompression. In these cases, the decompression speed is high, and the pressure near the crack will drop rapidly after a rupture. In cases where the fluid in the pipeline has a slow decompression wave, or the decompression wave has been delayed, there is a risk of running ductile fracture[3].

In the process of CCS, CO_2 is transported in a liquid or dense-liquid phase in the pipelines [5]. When a rupture occurs in the pipeline, the liquid CO_2 expands, which again leads to a phase change[20]. The CO_2 will begin to boil, and the fluid will consist of a mixture of liquid-phase and gaseous-phase CO_2[20]. The decompression speed of the liquid-phase CO_2 is higher than the speed of a ductile fracture. The CO_2 between the primary decompression wave and the crack tip will have a two-phase state, and the pressure present will be equal to the pressure of boiling CO_2[20]. Additionally, the two-phase fluid will create a different depressurization gradient from the one obtained in natural gas. While natural gas has a smooth depressurization, CO_2 will depressurize in a non-linear manner[5]. All these effects should be incorporated in the designing of pipelines used for CCS. The above explained factors of an RDF is presented in figure 2.1. Note that the figure only contains the fracture propagation in one direction, and that during an RDF, the fracture will propagate in both directions from the initial rupture[5].

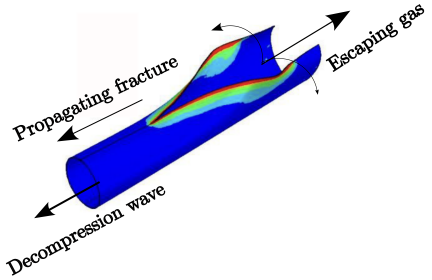

Figure 2.1: Figure adapted from [21]

2.2 Ductile tearing of pipes

Generally, materials can fail in two ways, brittle or ductile. Metals will typically have ductile fractures, with large plastic deformations. Ductile tearing of pipes has previously been studied by Schindler et al. [8]. Ductile fracture in pipelines is characterized by crack flanks opening, bulging at the crack tip and plastic deformation in the area of the flaps[22]. A brief summary of the governing mechanisms of ductile tearing, as presented by Schindler et al., is given in the following. In thin sheets, ductile tearing can be characterized by the creation of a crack-tip opening angle (CTOA), α. The CTOA tends to become constant after a minimum distance of crack propagation [23]. The ductile fracture in elastic-plastic sheets can typically be created by two specific load cases: stretching and bending. When a thin plate is subject to stretching necking will occur in the fully-plastic ligament. As

the crack extends, the strains on the entire ligament will increase and the fracture is eventually caused by plastic shearing. In the case of bending in the thin sheet, necking in the ligament is restricted to an area between the centre of rotation and the crack tip. The adjacent area is subject to compression which results in plastic swelling. For both loading conditions, the energy input required for the ductile tearing depends on the geometry and loading case of the deformed body.

Several different features are present in ductile tearing of pipes, compared to ductile tearing in thin sheets. For ductile tearing over a large axial distance to take place in a pipe, constant CTOA is necessary. A constant CTOA requires bulging ahead of the crack tip. Furthermore, for the creation of a bulge, plastic stretching of the material is necessary in the area near the newly formed crack. Additionally, necking occurs in a flattened zone ahead of the crack. The necking process is not a continuous process in the case of pipelines and has to be considered a plastic pre-deformation. The necking is largest at the crack tip and decreases in the area behind. A fracture process in the pipeline is considered to start when the bulge reaches the necked zone. The necking prior to the fracture ahead of the crack will ensure that the crack has a straight crack path in the axial direction. If the necking in the area ahead of the bulge is insufficient, the crack will have a lateral deviation, denoted "ring-off". This can happen if the crack propagation speed is slower than the sonic speed of the medium, and the phenomenon is often observed right before the crack-arrest.

2.3 Modelling of Running ductile fracture

Dynamic ductile fracture is a complex phenomenon that requires the utilisation of various analytical and numerical methods. Finite element methods (FEM) have been used to simulate the propagation of dynamic ductile fractures[16]. One widely used damage model for predicting ductile failure initiation and propagation is the Gurson-Tvergaard-Needleman (GTN) model[24, 25]. The GTN model is able to capture the complex behavior of materials undergoing ductile deformation and failure. The GTN model incorporates the concept of voids or pores within the material, which are crucial in influencing its mechanical response[16]. These voids act as nucleation sites for cracks, leading to the formation and propagation of fractures. However, the GTN model's accuracy is highly dependent on the mesh size and type used in the simulation, requiring fine discretization to obtain satisfactory results[16]. In the thesis conducted by Burchardt and Saether [17], the primary objective was to create a simplified model for propagating ductile fractures. The GTN model had been previously calibrated for various steel alloys used in pipelines, with the initial porosity as the only adjustable parameter. The calibrated GTN model was validated in the thesis, and satisfactory results were obtained. To address the challenges posed by computational complexity and mesh dependency, a 2D plane strain model incorporating the validated GTN model was initially employed as a reference model. The ductility of pipeline steels imposed limitations on the length of the plane strain model. A simpler shell element was introduced to replace the 2D plane strain model. The shell element was calibrated and the calibrated parameters alone were sufficient for the shell element to accurately represent a propagating crack in small-scale pipeline models.

2.4 Existing fracture propagation control

Fracture propagation control is mainly focused on the design of pipelines with high tolerance to defects, thus minimizing the length of long-running ductile fractures[12]. Following, two categories of approaches used for maintaining fracture propagation control is presented.

2.4.1 Uncoupled Two-curve methods

To maintain fracture propagation control, pipeline design has previously commonly been based on the Battelle two-curve method (TCM). The method stems from the Battelle Memorial Institute from the 1970s [26]. A semi-empirical curve was created based on extensive experimental datasets for natural gases and fluids. Following is a summary of the two curve method, as given by Aursand et al.[5], Gruben et al. [3] and Higuchi et al.[7].

The TCM gives an estimate for the desired material strength in terms of the Charpy V-notch (CVN) values needed to arrest an RDF. The method relies on a fundamental assumption that gas decompression and the fracture resistance in a material are two uncoupled phenomena. The original TCM is based on an equation expressing the critical hoop stress for a material at the crack-tip, σ_a, for arresting a fracture:

$$\frac{1000\,\mathrm{CVN}\;E}{A_C\sigma_f^2\sqrt{R\cdot t}} = \frac{24}{\pi}\ln(\sec(\frac{\pi}{2}\frac{3.33\sigma_a}{\sigma_f})) \tag{2.1}$$

where A_c is the area of a Charpy Specimen, E is the material's Youngs modulus, R is the pipe radius, t is the wall thickness, σ_f is the equivalent flow stress of the pipe material and CVN is the charpy V-notch values. The arrest pressure is related to the critical hoop stress as $p_a = \sigma_a \cdot t/R$. The arrest pressure can then be defined as the following equation:

$$p_a = \gamma\frac{2t\bar{\sigma}}{3.33\pi R}\arccos[\exp(-\frac{\pi R_f E}{24\bar{\sigma}^2\sqrt{Rt}})] \tag{2.2}$$

where $\bar{\sigma}$ is the material flow stress and R_f is the Charpy plateau energy per fracture area. The parameters α, β and γ are specific quantities for different models. The fracture speed in the axial direction is derived from the speed of a propagating plastic wave:

$$f(x) = \begin{cases} \alpha\frac{\bar{\sigma}}{\sqrt{R_f}}(\frac{p}{p_a}-1)^{\beta}, & \text{if } p > p_a \\ 0, & \text{if } p \le p_a \end{cases} \tag{2.3}$$

The gas decompression speed is calculated for a stationary fluid experiencing a full-bore opening in one end. This means that the opening process is stationary, not a running fracture. The speed of the pressure level is given in equation 2.4:

$$v(p) = c(p) - |u(p)| = c(p) - \int_a^b \frac{1}{\rho(p')c(p')}\,dp' \tag{2.4}$$

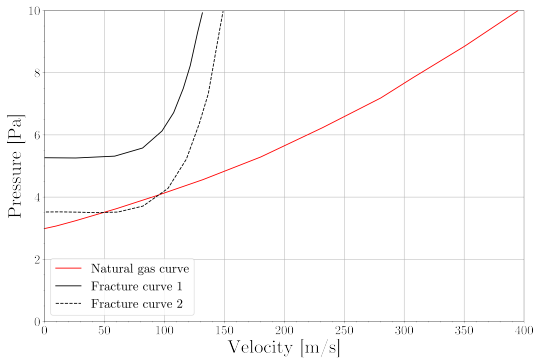

Figure 2.2: Examples of the two-Curve Method. Figures adapted from Gruben et al. [20]

For a multi-phase flow, no slip between the phases is assumed[5]. Figure 2.2 shows an example of a plot for the two-curve method[20]. The blue curves are fracture curves for two different material toughnessess. The red curve is the decompression wave for the fluid inside the pipe. The toughness of the material increases for a higher start pressure at the fracture curves. An arrest is expected for the fracture curve 1, and fracture propagation is expected for curve 2. As the TCM does not consider the two-phase characteristics of CO_2, an approach considering only the arrest pressure and the boiling pressure of CO_2 was suggested[3]. The crack arrest question relies upon the pipe's ability to withstand a propagating crack compared with the saturation pressure. The condition can be expressed as

$$p_s \leq p_a \tag{2.5}$$

where p_s is the saturation pressure for CO_2, and p_a is the arrest pressure for the material, as given in equation 2.2[3]. The TCM is empirically-based, and was developed using experimental data for vintage steel materials and natural gas. The method has proven to be non-conservative for the modern design of CO_2 pipelines [6, 12].

2.4.2 Direct Fluid-structure interaction models

A reason for the inaccuracy of the TCM is believed to be due to a lack of understanding of the factors governing the crack speed[14]. As the crack arrest question is determined by the race between the ductile fracture speed and the decompression wave, it is essential to predict the fracture speed. In modern pipeline design, pipelines have higher strengths and toughness, as well as lower pipe wall thickness[14]. Because of the high toughness, there are uncertainties regarding the relationship between the Charpy energy and the fracture speed[14]. Furthermore, to obtain an accurate description of the physical processes present during an RDF, a varying load in the area behind the crack tip has to be accounted for[27, 28]. The pipe will experience a variation in load due to depressurization and outflow of

the fluid[28]. Models where the computations of the fluid and the structure are coupled together are suggested as a solution for describing the acting pressure on the crack tip and the associated fracture speed[5]. The speed of the propagating crack is calculated from the fluid pressure acting on the crack. The pressure of the fluid is calculated using the surrounding geometry of the pipe as a boundary condition. Thus, an RDF can be described as a two-way coupled problem, known as coupled fluid-structure interaction (FSI) calculations[5].

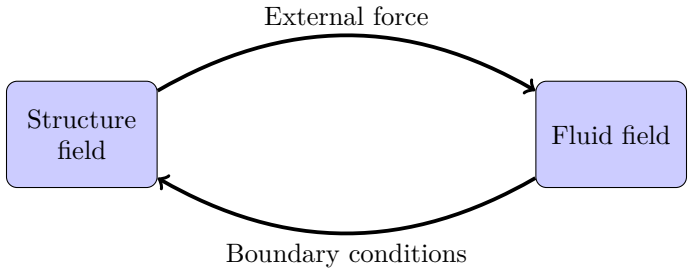

Figure 2.3: Caption

Hou, Wang and Leyton [29] has classified FSI approaches into monolithic approaches or partitioned approaches. In the monolithic approach, the same mathematical framework is used for the structure and the fluid. This will form one single equation set for the entire problem, which can be solved by an algorithm simultaneously. In a partitioned approach, the fluid and the structure are treated as two separate computational fields. These fields are solved separately with their respective discretizations and algorithms. For a partitioned approach, interfacial conditions are needed to communicate information in the coupling between the two domains.

According to Keim et al. [11], FSI approaches for fracture propagation simulation can be divided into to analytical models and finite element based models. For the finite element models, node-to-surface contact algorithms are often implemented[30]. A standard FSI algorithm for finite element models can be described by following scheme, as given by Rabczuk et al.[30]:

1. Surfaces and the belonging normals are computed
2. The fluid nodes that may come into contact with the surface are searched for
3. to prevent penetration of the fluid through the surfaces, penalty forces are applied to the fluid nodes

A set of rules and modification should be applied if the structure is allowed to fracture[30]. When using finite element methods for FSI, the flow through the opening crack requires communication of a defined crack shape. Hou, Wang and Layton [29] states that the structural domain is usually given in a Lagrangian description, while the fluid domain is often represented through Eulerian descriptions. The interaction between the flow and the structure can introduce issues, due to the coupling between the fields[30]. To overcome these problems, it is possible to use immersed particle methods and smoothed particle hydrodynamics (SPH). Smoothed particle hydrodynamics is a method where the fluid is

replaced by a set of particles[31]. By doing this, an approximate numerical solution for the fluid dynamical equations are obtained.

Previously, research on immersed particle methods for fluid-structure interaction and implementation of immersed particle model has been conducted by Rabczuk et al [30]. Following is a brief description of the key elements and attraction of using immersed particle methods. In an immersed particle method, the fluid and the structure are both treated by particles, removing the need for meshes. When using a mesh-free method for the fluid, the motion of the fluid through openings is naturally treated. The same algorithm can be used with and without crack present, and no modifications are needed for treating flow through voids. The fluid is treated by a Lagrangian description but can model considerable motions because of the use of particles. Research from Monoghan [31] on the application of smoothed particle hydrodynamics found that problems involving free surface disrupting can be simulated easily using SPH, while still giving satisfatory results. Additionally, SPH codes are considered easy to program, and can be used with little change for problems involving several fluids. In the work from Rabczuk et al., a method for immersed particles for simulation was implemented. The method was intended for problems with high-pressure waves on structures.

The coupled FSI methods are limiting, because these approaches are computationally demanding. Approaches based on FSI may require rich finite-element meshes or heavy 3D CFD computations or many-particles simluations, resulting in time consuming computations [5].

2.5 Effects of Backfill

Pipelines buried in soil or surrounded by water will experience external pressure from the backfill. The backfill is beneficial for resisting crack propagation[28]. The surrounding backfill will consume kinetic energy during the RDF, and dissipate energy from the expanding gas. This will result in a slower fracture speed and decreased fracture thoughness needed for the arrest of the RDF. [5] In the work by Gruben et al. [3] it was concluded that the submerged part of a pipeline was significantly less susceptible to RDF than the section located onshore. The effects of backfill have previously been studied for the damage process of an RDF [18, 32]. Furthermore, several studies has implemented particle models for representing backfill[11, 5]. The particles can represent granular materials experiencing large deformations, and will affect the design of a pipeline.

Chapter 3

Development of reference pressure decay model

The pressure of the CO_2 in a fractured pipeline have a strong spatial variation behind the crack tip [19]. This section contains some previously proposed pressure models and research with regards to spatial pressure decay in pipelines. Further, experiments and validation of a coupled fluid structure model is presented. The values obtained through the numerical models and simulations will lay the foundation for the development of a pressure decay model. The developed model will be implemented in simulations of the pipeline in chapter 4.

3.1 Modelling of pressure

One of the main issues with numerical simulations of running ductile fracture is defining the local pressure decay near the crack-tip region [14]. Although it is reasonable to assume the fluid flow ahead of the crack tip to be a one-dimensional flow, the same assumption cannot be made for the area behind the crack[33]. Research from experimental tests has found that there is a difference of more than 50% in pressure between the top of the pipe and the bottom of the pipe[5]. When a fluid storage component has sustained a fracture, complex three-dimensional transient flow exists until depressurization is complete [19]. Research and development of coupled FSI models have been based on the assumption of homogeneous equilibrium models and compressible one-dimensional fluid dynamics[5, 22, 34]. The process of depressurization in the crack tip region is considered to be dynamic, and the local pressure distribution behind the crack will determine the propagation of the fracture. From full-scale tests, it is known that the pressure profile on the crack tip can be captured in two dimensions. However, currently there are currently no direct methods for calculating such pressure profile behind the crack[28]. Several fluid models aim to describe the crack driving force, and will be presented in the following.

3.1.1 Two-curve method

The pressure calculated in the original two-curve method estimated the pressure at the crack tip as a function of the crack speed[19]. The equation for the pressure at the crack tip is given in 3.1.

$$p(V) = p_L(\frac{2}{\gamma+1} + \frac{\gamma-1}{\gamma+1} \cdot \frac{V}{C_L})^{\frac{2\gamma}{\gamma-1}} \tag{3.1}$$

In the equation, V is the crack velocity, C_L is the acoustic velocity at the initial operating pressure, p_L and γ is the ratio of the specific heat at constant pressure to the specific heat at constant volume. The equation is a homogenous one-dimensional equation and does not account for any spatial variations[5]. Equation 3.1 is also based on the assumption that the local sonic speed of a single-phase gas at the open end equals the local particle velocity relative to the moving fracture[3].

3.1.2 Spatial decay model

As experimental full-burst tests have shown that the pressure of CO_2 in a pipeline during RDF has a strong spatial variation[19], research and development of models accounting for the phenomenon has been conducted. Shim et al. [27] developed an exponential function for spatial pressure decay based on experimental full-burst tests. The research did not consider a coupling between fluid and structure, only the pressure as a function of the 3D position in the pipe. The model is divided into two sections divided by the current axial position of the crack tip. For the section ahead of the crack tip position, the pressure was assumed to be equal to the crack tip pressure. For the area behind the crack tip, the pressure varies based on the circumferential variation and the position with regard to the crack.

The developed pressure decay model is an exponential function that aims to describe the pressure in the area behind the crack tip. The model was developed from an experimental full-burst test of a pipeline. The experimental full-burst tests contained measurements for several circumferential positions, and linear interpolation was used to determine the pressure around the circumference. Shim et al. suggested a normalized pressure, given as an exponential function with the steady-state crack tip pressure p_0. The exponential function is scaled by a funciton of the circumferential position, θ, and the normalized distance to the crack tip, $\frac{z}{D}$.

$$p = p_0 \cdot \exp(f(\theta) \cdot \frac{z}{D}) \tag{3.2}$$

3.1.3 Keim et al

The equation from Shim et al. has been further developed and elaborated in the research by Keim et al.[35]. From equation 3.2, the exponential equation is scaled based the two directions: circumferential direction of the pipe cross-section ξ and axial direction along the pipe stoke x. An initial global pressure decay is developed based on experimental data.

The inital global pressure decay from initial pressure $p_{i,g} = p_{i,0}$ down to $p_{i,g} = 0.4p_{i,0}$ for the first $t_d = 20ms$ of the simulation. This decay is expressed as:

$$p_{i,g} = p_{i,0} \cdot (1 - \frac{0.6}{t_d} \cdot t_{sim}) \tag{3.3}$$

Following the global pressure decay, the proposed exponential function for the spatial decay behind the crack is given as:

$$p = p_{i,g} \cdot \exp b_1 \frac{x_{crack}}{x - l_{ref}} \cdot [1 + (\frac{4}{\pi} \tanh^{b_2}(\frac{\xi}{\pi}))] \tag{3.4}$$

The axial variation $f(x) = \frac{x_{crack}}{x - l_{ref}}$ is derived using the distance between the current position of the crack tip and the integration point, x_{crack}. The circumferential variation $f(\xi) = [1 + (\frac{4}{\pi} \tanh^{b_2}(\frac{\xi}{\pi}))]$ considers the angle ξ from the bottom of the circumferential cross-section of the pipe to the top. The axial function contains the reference length for the pressure decay, l_{ref}. Additionally, the equation includes two phenomenological parameters, b_1 and b_2. These parameters have previously been identified by Völling et. al. [28], which are based on experimental observations from Berardo et al.[36]. Ahead of the crack, the pressure is assumed to be equal to the global pressure, $p_{i,g}$

3.1.4 Xue et al

Further research from Xue et al.[37] aimed to research the anisotropic effects on crack propagation. The research implemented the pressure model from Keim et al, with modifications. The model developed considers the same time-dependent global pressure decay for the first 20 ms of the simulation. The axial scaling in equation 3.4 has been modified, and the equation from Xue et al. is given as:

$$p_{i,f} = p_{i,g} \cdot \exp(-b_1 \cdot \frac{l_{crack} - x}{l_{ref}} \cdot (1 + [\frac{4}{\pi} \cdot \xi \tanh^{b_2}(\frac{\xi}{\pi})])) \tag{3.5}$$

where l_{crack} is the length of the crack measured from the initial start point and x is the axial position on the pipe behind the crack. The equation contains the same phenomenological parameters b_1 and b_2, and the reference length for the pressure decay l_{ref}.

To get an overview of the pressure variation inside a pipeline, equation 3.5 has been plotted for varying axial and circumferential positions in a three dimensional space. The equation has been plotted for a given crack length l_{crack} and with the position x varying from 0 to $x > l_{crack}$. The parameter ξ varies between 0 and π. The reference decay length has been set to $1.2 \cdot$ Outer Diameter (OD). Furthermore, the crack distance, l_{crack} has been set to 3·OD. The decay model has been plotted for the normalized pressure, $p/p_{i,g}$. For an axial position, x, close to the crack, the pressure is close to the global pressure in the pipeline. The pressure ahead of the crack is equal to the global pressure, and decays in the area behind the crack tip. The circumferential scaling has a larger effect for positions further away from the crack tip region, where the crack has experienced larger deformations.

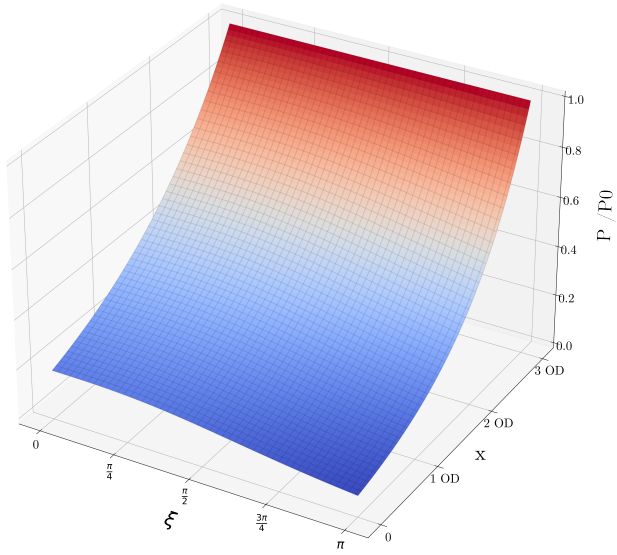

Figure 3.1: Pressure plot

3.2 Experimental data

The development of new numerical models and re-calibration of existing design models require full-scale test data which can represent the situation during the operational phase of CCS [20]. The execution of full-scale test data for CO_2 pipelines requires a lot of resources, and the data available are rather scarce[3]. Four projects over the last decade have produced experimental data for running ductile fracture. These four projects lie the ground for the validation and development of new numerical approaches to accurately describe the RDF phenomenon [3].

One of the experimental medium-scale burst tests conducted is the joint industry project CO2PIPETRANS[20]. The aim of the experiment CO2PIPETRANS was to check if the current design standards for fracture propagation control based on the two curve methods agreed with the observations. Further, a study done by Aursand et al. [5] aimed to validate a coupled fluid-structure interaction model, based on the data from the medium-scale test. This section covers the set-up of the CO2PIPETRANS experiment and the coupled FSI model subject to verification. The results from the simulations of the coupled fluid-structure model are presented. These results will lay the foundation

for the development of a reference pressure decay model, which will be applied in new simulations of RDF in pipelines.

3.2.1 Test layout and results

Following is the description of the test set-up of the experiment CO2PIPETRANS. The experiment aimed to test fracture propagation control based on TCM, where two tests were conducted. In the first test, no-arrest was predicted, while in Test 2, the crack would self-arrest. Further, in order to check several materials using the TCM, the pipeline consisted of different materials and geometries. The two tests had approximately the same test layout. The initial state of the CO_2 was changed between the two tests, in order to ensure arrest in the second test. This was done by changing the initial temperature of the CO_2, resulting in a two-phase fluid at a different saturation pressure.

The pipe consisted of four sections, two in each direction, West and East, and numbered as shown in figure 3.2. In the pipe stokes W1 and E1, the pipe stokes were supposed to propagate in test 1 and arrest in test 2. The two outer stokes, W2 and E2, were acting as gas reservoirs, and intended to ensure that the crack would arrest. For these stokes, the pipe is fully submerged in 1 m of sand backfill and the pipe walls are thicker than of the stokes further inn . For the pipe stokes W1 and E1 compact sand is surrounding the pipe up to the height of half the pipe diameter. To restrict any horizontal movement, two concrete blocks have been set up at the end of the pipes. In order to create the initial fracture in the pipe, a shaped charge was positioned on the centre girth weld in the axial direction.

To measure the pressure in the pipeline, the two tests were instrumented with calibrated pressure transducers positioned in the axial direction. The pressure transducers were positioned at a 3 o'clock position, at 1, 3, and 5 m in each direction from the axial midpoint of the pipe. Additionally, timing wires were mounted in order to track the propagating crack, thus being able to calculate the fracture propagation velocity.

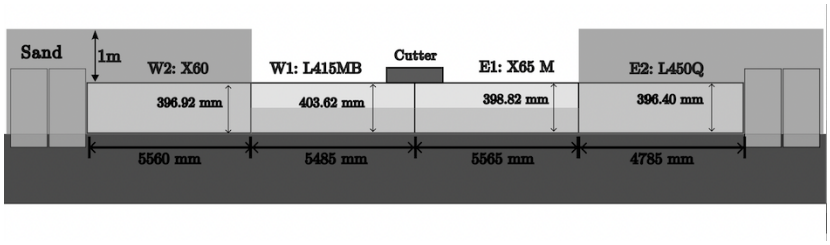

Figure 3.2: Test layout for the experimental full-burst test. Figure adapted from Aursand et al.[5]

As the development of a pressure decay model is based on the assumption of running ductile fracture, the results and conditions from Test 1 will be presented. A running ductile fracture propagated through the test pipes W1 and E1, and arrested when the crack reached the welds to the pipe stokes acting as gas reservoirs. A ring-off mechanism

was observed as the crack arrested. Table 3.1 contains a summary of the test conditions and results from Test 1.

Table 3.1: Conditions and results for the first test of CO2PIPETRANS. Table adapted from Aursand et al. [5]

Test	$p_i(bar)$	p_{sat} (bar)	Pipe stoke	Avg V_f ms^{-1}	Crack length (m)	t_a (ms)
Test 1	88.5	64	West 1	185	5.08	27.5
			East 1	135	5.16	34.4

3.2.2 The coupled model

In the research from Aursand et al., a coupled FSI model is subject to validation. In the research, a partitioned FSI approach is implemented, where the fluid and the structure are treated as two separate fields. The coupling between the fluid and structure is done through interfacial conditions. The following steps can summarise the coupled FSI model proposed:

1. The structure model communicates the current fracture width profile $w_e(x)$ to the fluid model
2. The fluid model uses this profile to integrate the fluid state for the current time
3. The pressure profile for each cross-section along the pipe length for the current time is communicated back to the structure model
4. The structure model uses the pressure profile at the current time to apply a load to its elements, and integrates the equations of the pipe material to the next time step.

The deformation and fracture of the structure have been modelled using shell elements and an elastic-visco-plastic constitutive equation. The structure model is implemented in the finite element program LS-DYNA [38]. All the elements of the shell model obtained in the simulations have the same fracture criterion and fracture parameters.

The fluid is modelled as a one-dimensional compressible flow of pure CO_2 using the homogeneous equilibrium model (HEM) and the Span-Wagner reference equation of state (EOS) [39]. The equation of state is possible to use for multi-phase flow under the assumption of no velocity difference between the phases[6]. The flow model can be written as:

$$\begin{aligned} \frac{\partial \rho}{\partial t} + \frac{\partial \rho u}{\partial x} &= -\xi \\ \frac{\partial \rho u}{\partial t} + \frac{\partial \rho u^2}{\partial x} &= -u_{x,e}\xi \\ \frac{\partial E}{\partial t} + \frac{\partial([E+p]u)}{\partial x} &= -(h_e + \frac{1}{2}u_e^2)\xi \end{aligned} \tag{3.6}$$

where x is the axial position, t is the time, ρ is the density of the fluid, u is the velocity of the fluid in the axial direction, p is the pressure and E is the total energy per volume. The factor ξ is an escape quantity describing the rate of mass loss per volume. The fluid model has been implemented using computational fluid dynamics (CFD). In the implementation of the one-dimensional fluid-model, two components are calculated at each axial computational cell. First, the cross-sectional average pressure p is calculated. Additionally, the escape pressure through the leakage in the pipe is calculated. The escape pressure represents the pressure at the fracture.

To properly account for the observed decrease in pressure from the bottom of the pipe to the top of the pipe, a circumferential variation has been proposed in the coupling scheme. Ahead of the crack tip, no circumferential variations are observed experimentally, and a calculated average pressure p is applied to all elements. Behind the crack tip, the cross-sectional geometry is considered. At each axial position behind the crack, the structure model communicates the fracture width $w_e(x)$ corresponding to the escape area A_e, and the largest width of the cross-section, $w_M(x)$. For the elements below $w_M(x)$, the average pressure was applied. For the elements above $w_M(x)$, an improved load estimate is applied, using the average pressure and the escape pressure. By considering different cases of the cross-section, the pressure model includes the spatial variation observed experimentally.

The fluid-structure coupling scheme has not been developed for the change of the crack direction and does not account for the observed ring-off that happens before the crack-arrest. Moreover, interactions from the geo-materials on the structure and on the escaping fluid will take place. For the interaction between the structure and the backfill, smoothed particle hydrodynamics has been implemented in the simulations. The interaction between the escaping fluid and the backfill has not been considered.

3.2.3 Results

Following are the results from the numerical simulations, as well as the results from the experimental tests. The dashed lines represents the experimental tests and the solid lines are the results from the coupled fluid-structure interaction model. The results of the simulations for Test 1 are said to be have an excellent agreement between the simulated data end the experimental crack speed, and additionally between the simulated and experimentally measured pressures.

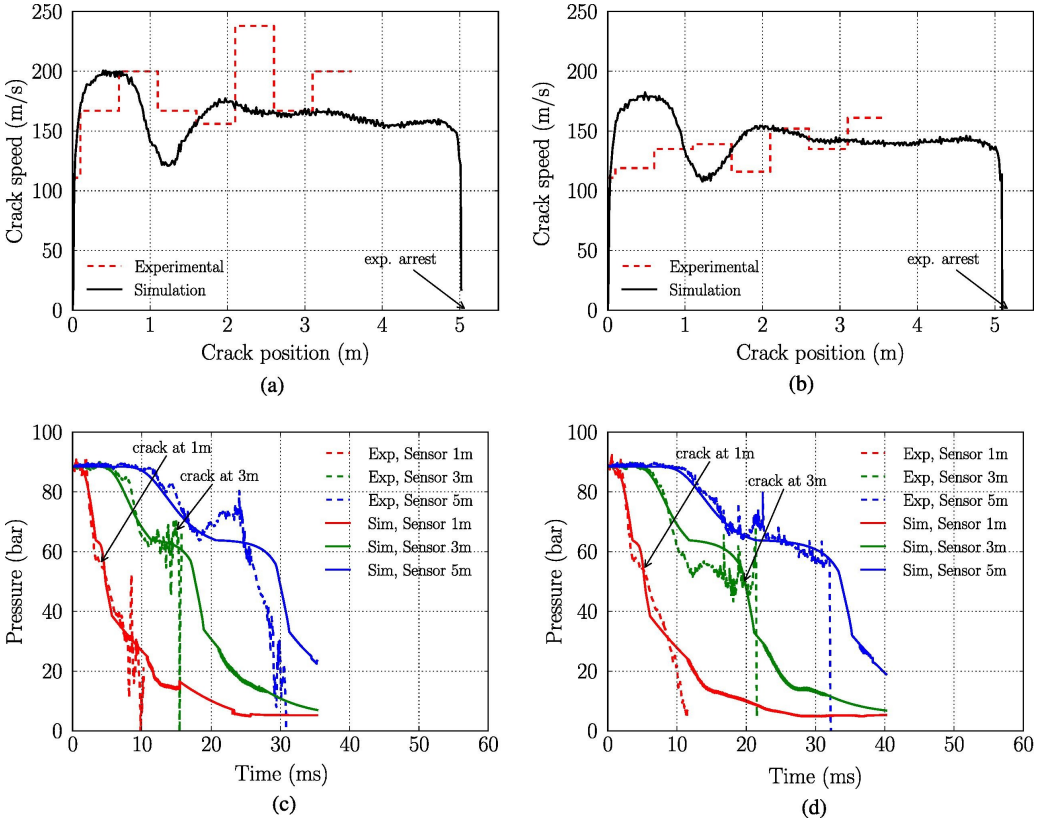

Figure 3.3: Result for test 1. subfigure (a) and (c) are the crack speed and pressure measurements for W1 respectively. Figure (b) and (d) are the same plots for pipe stoke E1. The plotted results are adapted from Aursand et al. [5]

3.3 Reference pressure decay model

This section covers the development of a reference pressure model. The model is developed using the results from Aursand et al, presented in 3.2.3, and based on the spatial decay models from Xue et al. and Keim et al. presented in section 3.1. As the development of a pressure decay model intends to model the pressure under a running ductile fracture, only the results from Test 1, where a running ductile fracture was observed experimentally, will be used. Furthermore, the results from the two pipe stokes W1 and E1 both have good agreement with the experimental values, and for the further development only the results from pipe stoke W1 is used.

3.3.1 Primary investigation

Primary investigation of the applicability of a spatial decay model has been conducted. In the primary investigation, the models from Xue et al., given in equation 3.5, and Keim et al. given in equation 3.4, are plotted for the sensors from the experiments. As the models expresses the pressure variation behind the crack tip, the models have been plotted for when the crack has surpassed the sensor position. The models do not take the area ahead of the crack tip into account and the global pressure ahead of the crack tip is set to $p_{i,g} = 0.4 \cdot p_{i,0}$. Furhtermore, the spatial models have been plotted for a varying crack position. The pressure model has been plotted against the experimental values, where the crack position is calculated using the average speed of the crack. The phenomenological parameters b_1 and b_2 have been set to respectively 0.69 and 2.9, as identified by Völling et al [28]. The reference decay length, l_{ref} has been set to $l_{ref} = 1.2OD$, as found by Völling et al. and presented by Keim et al. [28, 35]. The values used in the primary investigation are given in table 3.2.

Table 3.2: Values used for the initial investigation

$P_{i,g}$ (bar)	V_f (ms^{-1})	ξ	b_1	b_2	l_{ref}	OD (m)	l_{tot}(m)	l_{crack} (m)
88.5	$185 \cdot 10^{-3}$	$\pi/2$	0.69	2.9	1.2· OD	0.403	5.485	5.08

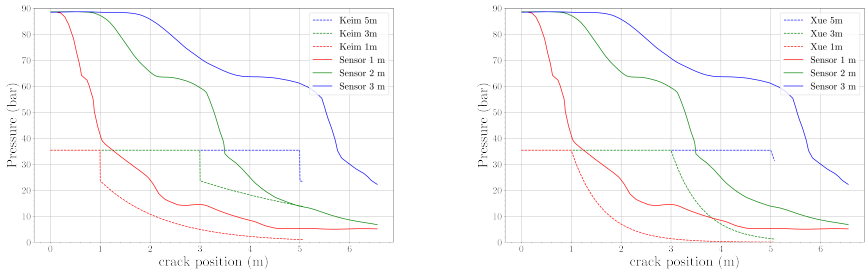

(a) (b)

Figure 3.4: (a) Model from Keim (b) Model from Xue

Figure 3.4 displays the initial plotting of the curves. It is evident that the curves have a poor fit, with a lower starting point and ending point. By studying the curves from the simulations in figure 3.5, some observations are made.

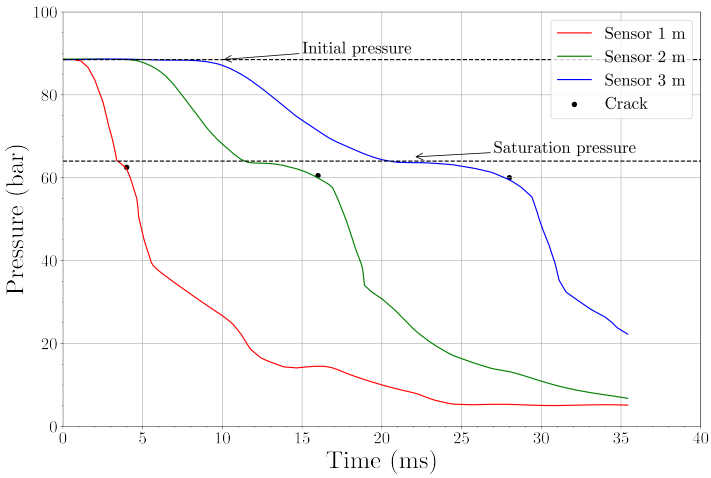

Figure 3.5: Original data from Aursand

1. Each of the curves has a plateau at the beginning of the curve, where the pressure is equal to the initial pressure
2. Following this plateau, the pressure rapidly drops down to approximately 64 bars
3. A new small plateau is placed around 64 bars
4. The points annotated 'crack' is where the crack has reached the sensor. All crack points infere with pressure near saturation point
5. The curves experience a second decay after the crack. For the sensors placed at 1 and 3 meters, the pressure decays to approximately 5 bar.

The pressure decay model are not able to capture all the variations observed in the simulations from Aursand et al., and has to be developed by accounting for the physical properties of CO_2 during a running ductile fracture. Furthermore, both section of a running ductile fracture, behind and ahead of the crack, should be investigated.

3.3.2 Initial depressurization

From the observations in figure 3.5, a primary pressure decay is observed from initial pressure down to approximately 64 bars. During the decompression of dense-phase CO_2, the fluid will enter a two-phase state, where the pressure of the fluid will be equal to the boiling pressure for pure CO_2. This is also known as the saturation pressure, or the plateau pressure, of CO_2 [20]. Under the conditions of Test 1, the saturation pressure for

the CO_2 is at 64.0 bars. The primary pressure decay may be related to the decompression wave of CO_2. The decompression wave of CO_2 travels down the pipeline with a speed V_w. As an RDF is present in the simulation, the speed of the decompression wave is higher than the crack speed V_{crack}. In order to investigate the effects of the decompression wave and the effect of the propagating crack, the curves have been adjusted with regard to the time. The adjustment uses the position of each of the sensors, and the speed of the decompression wave and the crack speed. Equation 3.7 represents the adjustments in time for when the decompression is experienced at an axial sensor position x. Equation 3.8 represents the adjustment in time for the curves for when the pressure decay related to the crack starts.

$$t_w = t - \frac{x}{V_w} \tag{3.7}$$

$$t_c = t - \frac{x}{V_c} \tag{3.8}$$

Figure 3.6 displays the simulated pressure curves, where the time has been adjusted. When adjusting the time with a constant speed for the decompression wave $V_w = 525$ m/s the pressure curves, independently of sensor placement, start to decay from the initial pressure. When adjusting the time with a constant speed for the running crack $V_c = 185$ m/s the pressure curves start to decay from approximately the saturation pressure for all sensors.

In order to model the initial pressure decay, a model based on the axial position of a sensor, x and the time t, as well as the speed of the propagating wave, V_w, of the CO_2 is suggested in 3.9.

$$p = p_i - (p_i - p_{sat}) \left(1 - \exp\left(-k \left\langle t - \frac{x_s}{V_w} \right\rangle\right)\right) \tag{3.9}$$

Here, $p_{i,0}$ represents the initial internal pressure of the pipeline and p_{sat} is the saturation pressure. The parameter k is an adjustment parameter. The equation includes the Macauley brackets for the term of the adjusted times. Macauley brackets describe a ramp function. If the term $t - \frac{x_s}{v_w}$ is negative the value inside the brackets is set to 0. When plotting the initial decay against the values, the parameter k has been fitted for the curves. Table 3.3 gives an overview of the obtained values for the three sensors placed at 1, 3 and 5 meters.

Table 3.3: The constant k used to describe initial pressure decay

Sensor	1m	3m	5m
k	1.0	0.35	0.18

Figure 3.7 displays equation 3.9 plotted against the values from the simulations. The developed model is close to the simulated values, and is believed to be a good description of the event happening after a tear in a pipe.

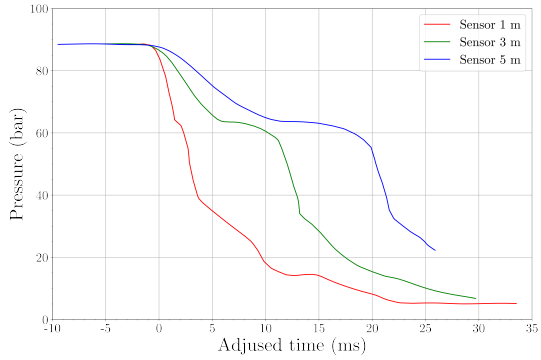

(a)

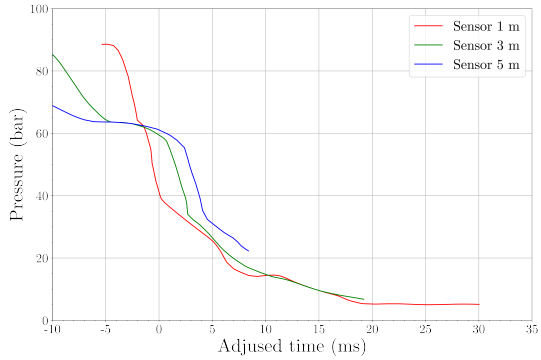

(b)

Figure 3.6

3.3.3 Circumferential variation

As mentioned in section 3.1, the pressure of the fluid will have a circumferential variation in the area behind the crack tip. The circumferential scaling is given as:

$$f(\xi) = 1 + [\frac{4}{\pi} \cdot \xi \tanh^{b_2}(\frac{\xi}{\pi})] \tag{3.10}$$

All predictions and measurements have been carried out at a 3 o'clock position on the pipeline. Thus, for the further development of a reference pressure decay model, the circumferential term is adopted. The value of ξ is set to $\pi/2$, which is the radial value for the 3 o'clock position. The parameter b_2 controlling the pressure distribution is set to 2.9 according to Völling et al. [28]. Figure 3.8(a) displays the circumferential scaling parameter for the different values of ξ. In figure 3.8(b) pressure curves are plotted for three different circumferential positions, at the sensor at 3 meters.

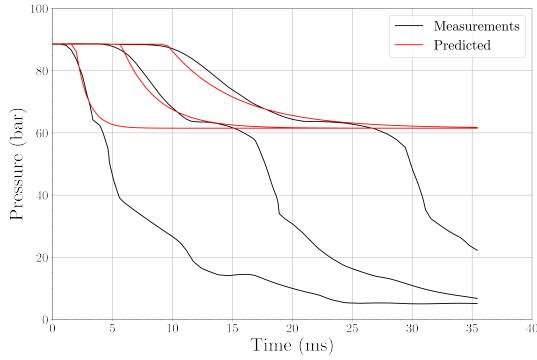

Figure 3.7: Pressure related to depressurisation of CO_2

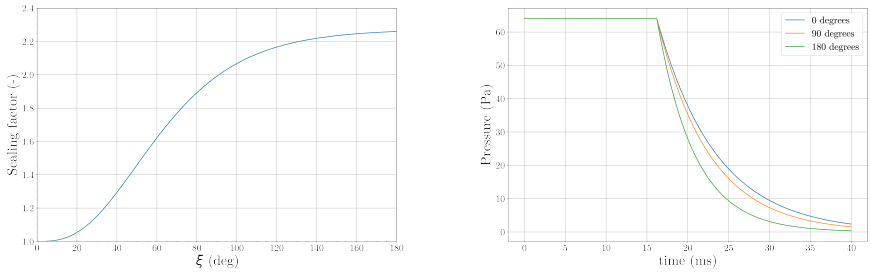

(a) (b)

Figure 3.8: (a) displays the circumferential scaling factor, $f(\xi)$. (b) displays the variation of pressure along the circumference for a sensor placed at 3 meters

3.3.4 Pressure related to crack

As seen in figure 3.6b, the pressure decay related to the crack take place after the pressure has reached a plateau at the saturation pressure. A spatial pressure decay model can be used from the area where the crack tip has reached the pressure sensor. The spatial decay model given by Xue et al. in equation 3.5 will be used to describe the spatial variation. The pressure model can be written as:

$$p = p_{sat} \cdot \exp(-a < x_c - x > (1 + \frac{4}{\pi} tanh^b(\frac{\xi}{\pi})) \tag{3.11}$$

where x_c is the position of the crack in the pipeline at a given time t, x is the position of the pressure sensor, and ξ is the angular position of the sensor along the circumference of the pipeline. The equation contains the parameters a and b, where the parameter a has been altered to include the reference decay length, l_{ref}. The parameter a has been adjusted to the pressure recordings. In order to study the pressure related to the crack,

without accounting for the initial depressurization, the curves have been plotted starting from a pressure equal to the saturation pressure. The decay starts from the time the crack has reached the sensor position and has been plotted for a time simulation equal to $t_{sim} = 40$ ms. Furthermore, the parameters have been set to $a = 0.75$ and $b = 2.9$, and the saturation pressure is $p_{sat} = 64.0$.

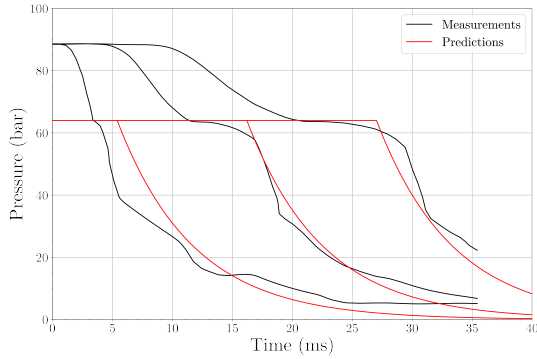

Figure 3.9: Pressure related to the running crack

3.4 Results

The postulated pressure model accounts for the initial depressurization wave propagating along the pipe ahead of the crack. Additionally, the spatial pressure decay behind the crack during a running ductile fracture in a pipeline is accounted for. The model created calculates the adjustment parameter k for the wave-related pressure decay based on the location of the sensor. The parameter k is calculated as:

$$k = \min\left(1.0 - a \cdot (1 - e^{-b \cdot (x - 1.0)}), 1.0\right) \tag{3.12}$$

where $a = 0.82$ and $b = 0.75$. The calculation ensures that the parameter k does not exceed the value 1.0. The complete model, containing both the initial pressure decay and the spatial decay, has been plotted for the three sensor positions in figure 3.10.

3.4.1 Varying axial positions

The obtained solution has been plotted for several sensor positions, in figure 3.11. This has been done in order to visualize the effects of the axial position on the pipe for the parameter k. The pressure decay related to the depressurization of CO_2 will have a gradually flatter curve.

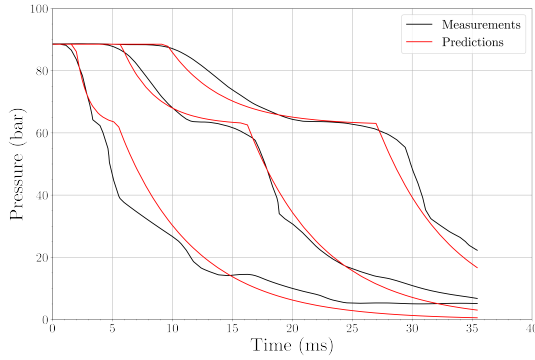

Figure 3.10: Full pressure model

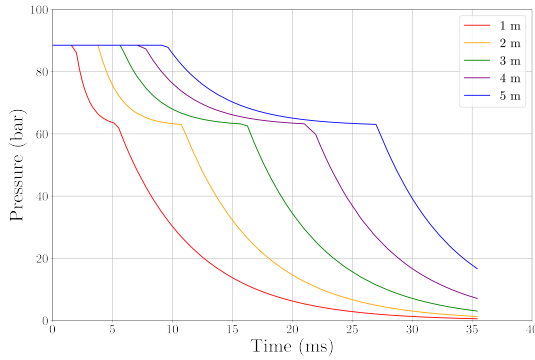

Figure 3.11: Developed model for different sensor positions

3.4.2 Variation of speed

The developed pressure model has been plotted for several crack velocities, for the sensor placed at 3 m. Figure 3.12 illustrates the effect the crack speed has on the developed model. The initial decay will not be affected by the crack speed. Only the crack-related pressure decay is altered when the speed is changed.

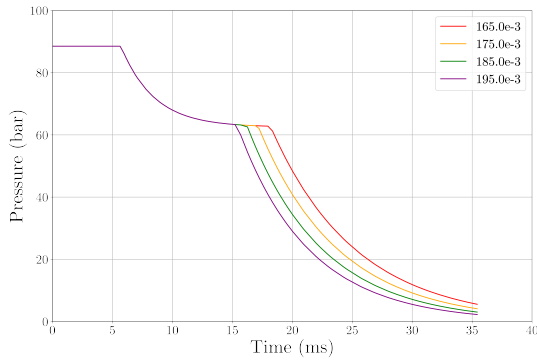

Figure 3.12: Developed model for different crack speeds for the sensor placed at 3m

3.5 Discussion

From the results in figure 3.10, it is observed that the developed pressure model has an overall good fit with the values obtained from simulation and experiments. Although the time-dependent global pressure decay presented by Xue et al. was not studied, the obtained solution is able to account for a global decay by incorporating the effects of the depressurization wave. The mechanism of the first decompression speed could be associated with the internal pressure trying to reach equilibrium from the initial pressure $p_{i,0}$, and the sudden pressure drop induced by cracking the pipeline. The variation of the parameter k in the depressurization could be related to the volume of gas being larger when increasing the distance along the pipeline. Furhtermore, for the pressure sensor placed at 1m, the pressure decay related to the crack has a smoother curve. It is possible that the simulated curves will have some variation due to the incorporated effects from backfill. Although the crack speed is varying, as seen in figure 3.3, the developed pressure curve use the calculated average speed given in table 3.1. The use of average speed is not considered to affect the obtained model particularly.

Chapter 4

Pipe simulation

In order to study the effects of the developed pressure decay model, a pipe containing a running ductile fracture has been simulated. The pipe has been implemented in the finite element program Abaqus [40]. The modelling of the pipeline is based on the thesis by Burchardt and Saether [17]. This section describes the modelled pipelines and the results from the simulations.

4.1 Method

The model of the pipe has been based on the experiment CO2PIPETRANS, and has been created using a provided Abaqus-script. Following is a description of the mesh, geometry, material, crack and load implemented through the script.

4.1.1 Pipe

The pipe has been divided into two pipe stoke sections, both with an initial length of 5500 mm. The two sections have been denoted first and second pipe. The two sections aim to model the layout for one of the directions in Test 1 of CO2PIPETRANS, where the second pipe acts as a gas reservoir. The first pipe has a wall thickness of 6.2 mm, while the second pipe has a wall thickness of 14.3 mm. The pipe model is meshed using S4R shell elements, with 5 through-thickness integration points. The elements have a length in axial direction equal to 10 mm, and a thickness equal to the pipe thickness. Furthermore, the material of the pipe is the steel alloy L415MB, as used in pipe stoke W1 in CO2PIPETRANS. A support plate has been included to model the compressed quarry. The second pipe has been constrained in all directions at the end to prevent displacement, modelling the concrete blocks on the end.

4.1.2 Crack

The modelling of the crack has been adapted from the work of Burchardt and Saether. In this work, the crack was modelled using special shell elements along the axial direction of the pipeline. The crack elements have a thickness equal to 6.2 mm and width and length

equal to 6.2 mm and 10.0 mm respectively. The elements representing the crack are S4R elements with 5 through-thickness integration points and have been assigned accelerated plastic thinning. The surrounding shells have been constrained from changing thickness. Additionally, the surrounding shells have no failure criterion and have been assigned a satisfactory work hardening model.

To simulate the beginning of a crack, initiated by an explosive cutter in the experimental full-burst test, the pipeline has been assigned an initial crack. The initial crack has a length equal to $l_{crack} = 2\pi \cdot D/2$, where D is the diameter of the pipe. The initial width is equal to the width of the crack elements, and set equal to $w_{crack} = 6.2$. The crack has been modelled to run with plane strain conditions, according to the plain strain and shell model from Burchardt and Saether. Although ring-off right before crack arrest is often observed in experimental tests, the simulation will only account for axial crack propagation along the top of the pipe. Figure 4.1 depicts a pipeline with an initial crack, seen from above. The elements in blue are the special crack elements.

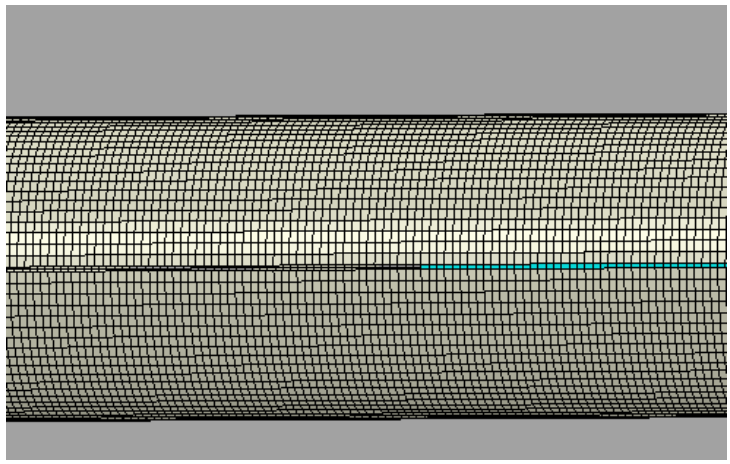

Figure 4.1: Pipe with the initial crack. The blue elements represent the crack elements along the 12 o'clock position

4.1.3 Load

Burchardt and Saether implemented a simple load model using uniform surface distributed load. An iterative scaling method was applied for the areas where the deformed pipe had developed opening flaps. This ensured that only a portion of the force was applied in the normal direction of the deformed elements. In the work, it was concluded that a more complex load model was needed. For the current model, the pressure model developed in chapter 3 is applied on the inner surface of the pipe. An explicit dynamic step has been used for the load. During the development of a reference pressure decay model, the pressure was given in Bar. In the simulations, the pressure will be given in MPa.

4.1.4 Geometries

The simulation of a running ductile fracture in a pipeline has been replicated for four different pipe geometries denoted pipe simulation 1, 2, 3, and 4. Pipe simulation 1 contains the geometry and materials from pipe stoke W1. In pipe simulations 2 and 3, the pipe diameter has been modified to be 200 mm larger and 200 mm smaller, respectively. By changing the diameter, it is possible to see how the pipe diameter affects the propagating crack and thus the pressure inside. Because the shell elements are of the same size for all the simulations, the number of elements along the circumference and the number of total elements will change accordingly. Lastly, for pipe simulation 4, the pipe was modelled such that no arrest is expected in the welds between the first and second pipe. By changing the thickness of the second pipe to the same thickness as the first pipe, 6.2 mm, the crack will propagate through the second pipe. Table 4.1 summarises the variation of the geometries of the different pipe stokes, as well as the number of active elements each model contains.

Table 4.1: The four different pipelines geometries

Pipe number	Diameter (mm)	n_E active elements
1	406	93372
2	606	135110
3	206	45035
4	406	93372

4.2 Results

Figures 4.2, 4.3 4.4 and 4.5 depict the deformations of the four pipelines, with the pressure acting on the deformed pipe. The crack propagates as expected for all the pipe simulations. In pipe simulations 1, 2, and 3 the crack arrest in the welds between the first and the second pipe. For pipe simulation 4, no arrest is present, and the crack has propagated through the second pipe. The pipe simulations obtain different simulation times. For pipe simulation 1, the simulation time was 32 ms, while the simulation times of pipe simulation 2, 3 and 4 were 14.5 ms, 50 ms, and 50 ms respectively. The difference in simulation time is a result of varying crack speeds due to varying pipe diameters. Gruben et al. state that a larger pipe diameter will result in pressure being applied on a larger area and the crack-driving force increases[3]. Thus, the simulation time will increase and decrease accordingly. The effect of varying diameters is further supported in the parametric study conducted in the thesis of Burchardt and Saether, where it was observed that the pipe diameter had a large impact on the crack speed.

The crack has some differences in the final deformations, although the base geometry is similar. At the end of the simulated RDF the material in pipe 1 will bulge on the bottom of the pipe near the pipe start. The same bulging is present and larger in pipe 2, and not present in pipe 3. The bulge could be due to the force applied in the pipe in combination with the crack arrest in the welds. Additional figures of the deformed pipes are enclosed in appendix A. The simulation has the desired physical representation of an RDF and data obtained from the output files are applicable for the training and validation of a machine learning model.

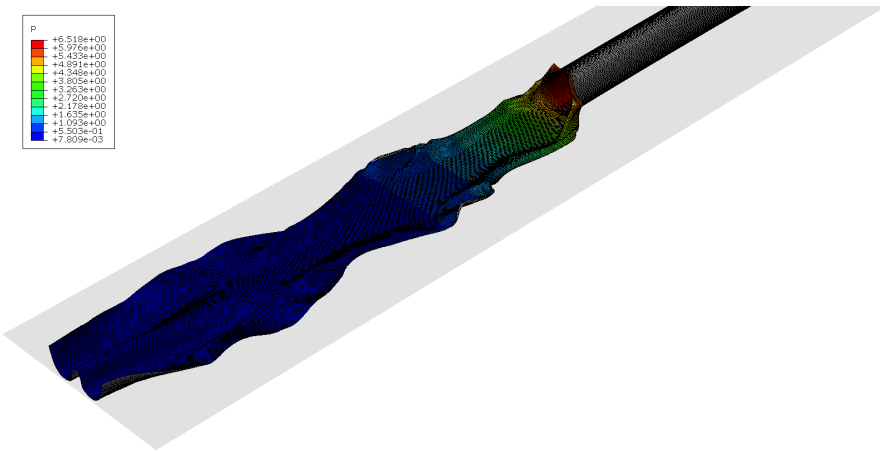

Figure 4.2: RDF in pipe simulation 1

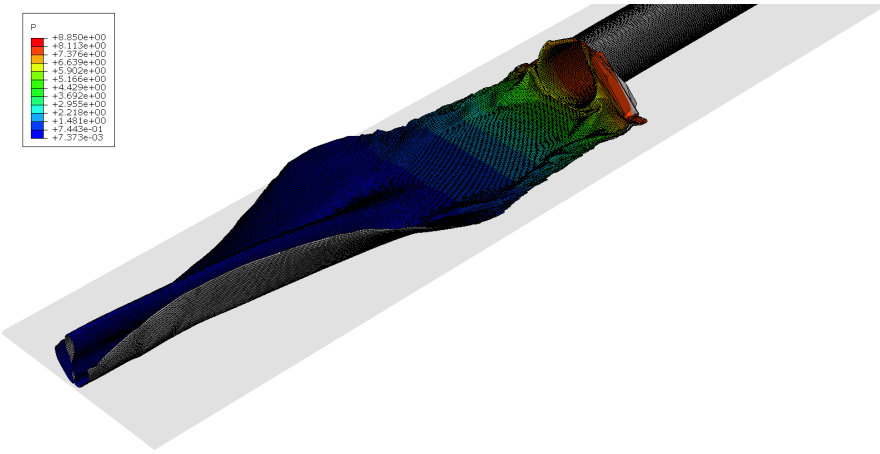

Figure 4.3: RDF in pipe simulation 2

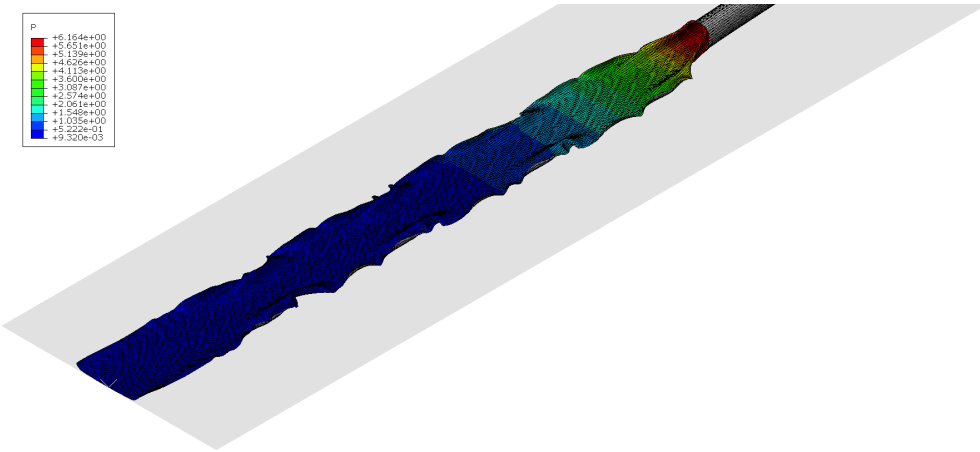

Figure 4.4: RDF in pipe simulation 3

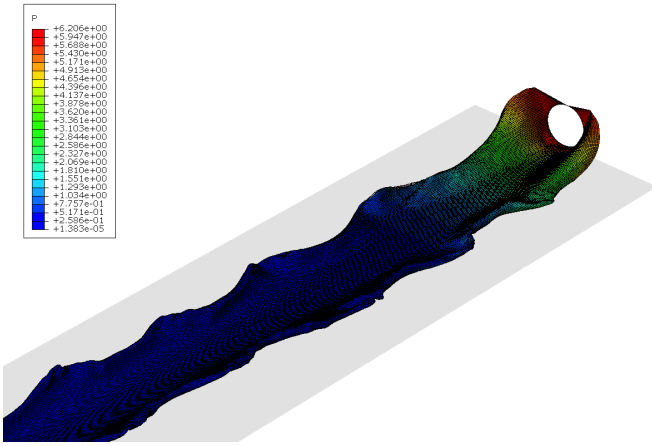

Figure 4.5: RDF in pipe simulation 4.

Chapter 5

Artificial Neural Network

This section covers background and theory behind artificial neural networks. The implementation of the neural networks is presented.

5.1 Background

Artificial neural network (ANN) is a type of machine learning model inspired by the structure and function of the human brain [41]. ANN consists of interconnected neurons that process information through a series of mathematical operations[42]. Each neuron takes in one or more inputs, performs a calculation and produces an output that is passed on to the next layer of neurons. A neural network is trained using a data set of input-output pairs, where the input represents the features or attributes of the data and the output represents the target or value aimed to predict[42]. ANN can be used for various tasks, including classification, regression, and pattern recognition. A network can learn to identify complex non-linear relationships between the input variables and the target variable, making it a powerful tool for prediction and forecasting[41].

According to Goodfellow et al.[41], machine learning algorithms can broadly be categorized into three different types; supervised and unsupervised algorithms, and reinforcement learning. In an unsupervised learning algorithm, the algorithm aims to find patterns based on the structure of the data provided. In a supervised learning algorithm, the algorithm aims to find structure between the features and the associated labels or targets[41]. In reinforcement learning, the algorithm continuously evaluates the results while learning, giving a feedback loop between the learning system and the experiences[41].

Traditionally, regression problems are referred to as supervised learning [41]. The data set is in the form of structured inputs and outputs, and the algorithm aims to model continuous variables. There are several types of algorithms for regression analysis, including the most simple algorithms like Ordinary least square (OLS) regression analysis. However, one of the issues with linear regression is that a linear relation is assumed. This may oversimplify real-world problems, and linear regression is unable to deal with the relationships or complex patterns of the data [41]. Neural networks use multiple simpler representations to describe and solve these complex concepts.

5.2 Theory

Following is theory behind neural networks used for regression analysis.

5.2.1 Feedforward neural network

Commonly, for regression problems, feedforward neural networks (FFNN) are used. A feedforward neural network is the simplest form of neural network, where the goal is to approximate a function f . These networks are characterized by their feedforward flow, which means information is passed strictly in one direction, without feedback connections[41]. In a feedforward network, a mapping is defined as $y = f(x;\theta)$. For the mapping, the network will learn which parameters of θ that result in the best function approximation[41]. The mapping makes FFNN suitable for tasks that require static inputs, such as regression problems[41].

5.2.2 Layers and Nodes

An artificial neural network consists of interconnected neurons, organized in several layers. Each neuron of one layer is connected to all neurons of the next layer[42]. Each neuron in an FFNN receives inputs from the previous layer, performs a weighted summation of the inputs, applies a non-linear activation function, and passes the output to the subsequent layer [43]. An FFNN typically contains an input layer, one or more hidden layers, and an output layer. The input layer accepts the input data, which in the case of regression problems are numerical values. Hidden layers enable the network to learn complex representations by extracting higher-level features from the input. The output layer produces the final prediction or decision based on the information processed through the preceding layers [41].

5.2.3 Training process

The training process of an FFNN involves two main steps: forward propagation and backpropagation [41]. In forward propagation, the input data is passed on through the network, and the activations of each neuron are sequentially computed. This is done until the output layer is reached[41]. This process generates a predicted output. To optimize the performance of a network, the predicted output is compared with the desired output using a loss function [16]. For regression problems where the output variables are continuous, the most common loss function used is mean squared error, MSE. The equation for MSE is given in 5.1.

$$MSE = \frac{1}{n}\sum(\boldsymbol{y} - \hat{\boldsymbol{y}})^2 \tag{5.1}$$

where y is the output obtained from the target, and $\hat{y}$ is the predicted output.

After calculating the initial prediction, the weights are updated iteratively by an algorithm denoted backpropagation[41]. By calculating the gradients of the loss function with respect to the weights, the algorithm adjusts the weights in a way that minimizes the loss.

This process is repeated over multiple iterations until the network converges to an optimal set of weights. One iteration can be denoted as an epoch.

5.3 Previous work

Although the use of artificial intelligence has gained increasing interest within the field of fracture mechanics in recent years[15, 16], research and applications of AI for running ductile fracture has been scarce. Paermentier et al. [16] have studied a machine learning sensitivity analysis for pipelines. In this research, an artificial neural networks was used to analyze and predict the fracture energy value for a set of given GTN parameters in X70 pipeline steel. The material-dependent parameters in the GTN model for one steel grade material can show a wide spread in the prediction of ductile fracture initiation. For training the neural network, seven different GTN parameters were used as input. The corresponding Charpy energy value is used as an output for the network. In the research, it was observed that the trained network could predict a satisfactory approximation of the Charpy V-notch fracture energy.

5.4 Data and variables

Following is a description of the generation of data, the correlation obtained through the data set and the pre-processing of data.

5.4.1 Data generation

The data was extracted from the simulations in Abaqus given in chapter 4. As previously mentioned, four different simulations were done, each considering different cases of pipe geometry. The data from pipe simulation 1 will be used for training, while the remaining pipe simulations will be used for testing.

From the simulation in Abaqus, data of five variables has been extracted for further use. Firstly, the data used for analysis consist of the time steps obtained in the simulation, t, and the position of the running crack at each time step, Z_c. Further the machine learning model should be able to detect the spatial variation within a pipeline. The data set denoted Z contains the position of an element at every time step. In order to account for the circumferential variation, the data denoted N contains the y-component of the normal vector of each element. The y-component of the normal vector will provide information of where along the circumference the element is placed. If the value is close to -1 the element is placed at the bottom at the pipe, while values close to 1 is near the top of the pipe. Lastly, data containing the pressure on each element at every time step is denoted P. All positional variables are given in millimeters, and P is given in MPa, and time is given in seconds.

The data for the circumferential position, axial position, and pressure are all built as matrices. Every column represents all the elements obtained in each simulation, and every row represents a time step of the simulation. In order to create a data set used for regression and machine learning, the data needs to be reshaped and concatenated.

The final data set used for analysis contains the five variables, where the number of data points is calculated as $n_{datapoints} = n_E \cdot t$.

5.4.2 Correlation study

A correlation study of the variables of the training data has been conducted. The correlation states the influence between the variables, and how the independent variables correlate to the dependent variables. The correlation between two variables is calculated using Pearson's correlation coefficient[44]:

$$r = \frac{\sum_{i=1}^{n}(X_i - \overline{X})(Y_i - \overline{Y})}{\sqrt{\sum_{i=1}^{n}(X_i - \overline{X})^2 \sum_{i=1}^{n}(Y_i - \overline{Y})^2}} \tag{5.2}$$

A strong correlation factor typically has values between ± 0.50 and ± 1, and indicates a close relationship between the variables. A moderate correlation factor typically lies between ± 0.30 and ± 0.50, where the independent variables will affect the dependent to some degree.

Figure 5.1 displays the correlations between the different variables of the data for the training, obtained from pipe simulation 1. From the heat-map, it is observed that between the input variables, the position along the axis of the pipe, Z, has the strongest correlation to the pressure, P. As the primary decompression from the pipe depends on the axial position along the crack, the pressure will become more influenced by the axial position Z along the pipe. The other variables, t, N and Z_c all influence the pressure equally. The correlation observed between the normal, N, of each element and the pressure can be seen as the circumferential variation previously discussed. It should be noted that as the data used for testing have been extracted from simulations of different pipeline geometry, the correlation matrices will differ. The correlation matrices for the data for pipe simulations 2, 3 and 4 can be found in the appendix B.

5.4.3 Data pre-processing

Data pre-processing plays an important role in ensuring the quality and reliability of machine learning models by addressing challenges such as missing data, outliers, and inconsistent formatting. All these factors can impact model performance. In the present case, there are no missing data or outliers. However, the data have inconsistent formatting. Table 5.1 describes the variation in the different variables, presented by the min and max values for pipeline 4, used for training. The corresponding tables for the testing data can be found in the appendix C.

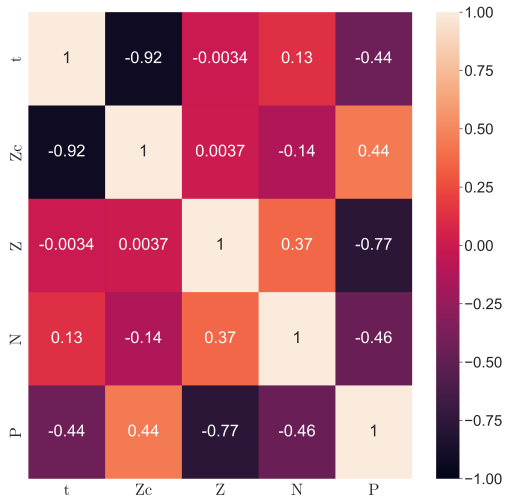

Figure 5.1: Pearsons correlation factor visualized as a heatmap between the different variables in the data set

Table 5.1: Value range for the variables of training data

Parameter	min	max
t (s)	0.0005	0.0320
Z_c (mm)	5359	9628
Z (mm)	4.964	10995
N	−1.000	1.000
P (MPa)	0.0078	8.850

As the values from the data set have very different minimum and maximum values, the data has been scaled to account for all values equally in the machine learning algorithm. Normalization of the data has been used, scaling all values of the variables to fit in the range between 0 and 1. This is done by applying equation 5.3 to all the variables of the data set.

$$\bar{X} = \frac{X - X_{min}}{X_{max} - X_{min}} \tag{5.3}$$

It is important to note that the scaling applied to the training set should be applied to the testing data as well. Further, the training data is split into training and validation data. The data has, with a random selection, been divided into training data containing 70% of the data, and the remaining 30% is validation data. As the data set contains a

large number of data points, a split of 70/30 is deemed appropriate.

From table 5.1 it is observed that the crack has a high minimum value. Further, the crack propagates a distance equal to approximately 4250 mm. In the tables for the value range for the test data a negative values are observed for the axial position Z. However, after data exploration of all the data sets, the data has been deemed as usable for training and testing machine learning models.

5.5 Implementation

This section covers the implementation of neural networks. The hyper-parameters, such as the number of nodes and layers, are presented for each model implemented. The training of the models is presented with regard to the loss and validation loss. For the implementation of the machine learning model, Python libraries Tensorflow[45] and Keras[46] have been used. The aim of the neural network is to be able to predict the pressure P, based on a set of input parameters. Figure 5.2 displays the general architecture of the implemented neural network. This section covers the models implemented, and the results of the training. The number of neurons, or nodes, and the number of layers will be modified, in order to find an optimal network architecture.

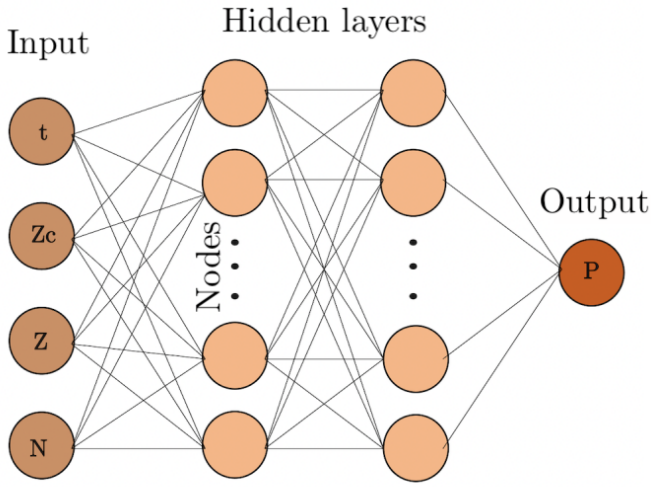

Figure 5.2: Architecture of a neural network for predicting the spatial pressure decay

5.5.1 Model 1

First a simple neural network has been implemented. The neural network consists of an input-layer, where the variables t, Z_c, Z and N are given as input. The neural network further consists of two hidden dense layers, with 64 nodes in each. The model was trained with a batch size of 64. The optimizer used was stochastic gradient descent with a

learning rate equal to 0.2. The activation functions used were rectified linear unit (ReLu) for the input and hidden layers, and a linear activation function for the output layer. Furthermore, early stopping has been implemented. This was done in order to ensure that the model finds the correct general representations and relationships, and not finds the best fit for the training data[42]. This phenomenon is denoted overfitting, and in this case the model will not be able to predict correctly for test data. The neural network ran for 14 epochs before early stopping was activated. The loss was calculated using MSE, and the training and validation loss are given in figure 5.3.

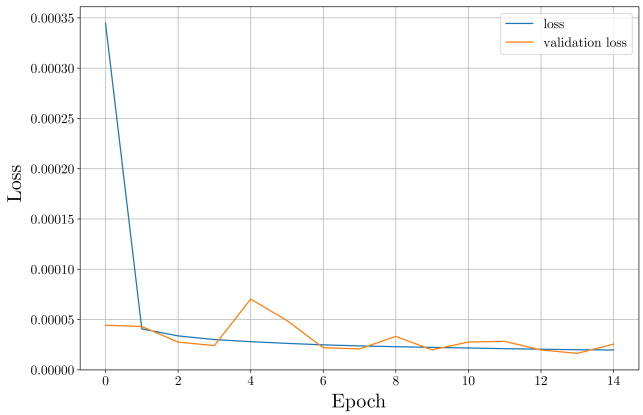

Figure 5.3: Loss model 1

5.5.2 Model 2

Model 1 was trained again separately but without early stopping. The aim was to test if the learning became any improved if the training was run for all the epochs, but with an increased batch size. The model was trained for 30 epochs, and with a batch size of 128. The same layer, nodes, and parameters for optimization were used as in model 1. Figure 5.4 are the graphs for the loss for the training and validation of model 2.

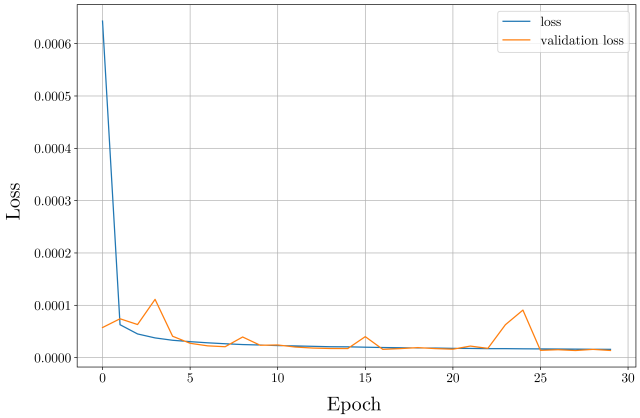

Figure 5.4: Loss model 2

5.5.3 Model 3

Further, a third model was implemented with 3 hidden layers and 64 nodes. The implemented model has been trained with early stopping and hyper parameters as in model 1. The aim was to see if adding one more layer would improve the training, resulting in lower loss. The network iterated through 19 epochs before early stopping was activated. The training and validation losses are plotted in figure 5.5.

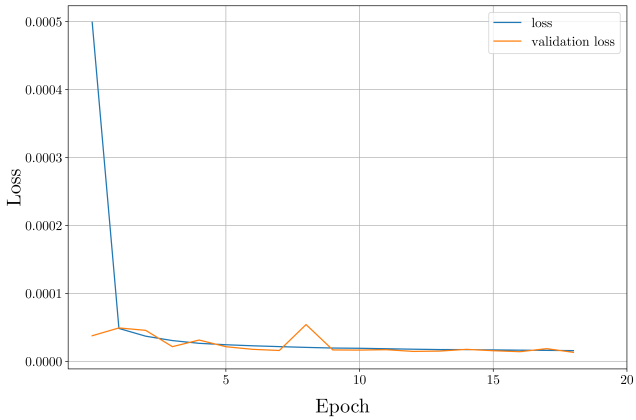

Figure 5.5: Loss model 3

5.6 Results

In order to validate the training from the machine learning model, the models have been used for prediction of the test data from pipe simulations 2, 3 and 4. The test data all represent three new cases for the machine learning model: larger and smaller pipe diameter, and longer fracture propagation.

5.6.1 Accuracy

In order to evaluate the goodness of fit from the different models, the R^2 score for each model on the test sets has been calculated. The R^2 score ranges between 0 and 1, and a value of 1 indicates a perfect fit. The R^2 score is calculated as:

$$\begin{aligned} R^2 &= 1 - \frac{RSS}{TSS} \\ &= 1 - \frac{\sum_{i=1}^{n}(y_i - \hat{y}_i)^2}{\sum_{i=1}^{n}(y_i - \bar{y})^2} \end{aligned} \tag{5.4}$$

where the TSS is the total sum of squares and RSS is the residual sum of squares. The value y_i represents the true values, $\hat{y}_i$ represents the predicted values, and $\bar{y}$ represents the mean of the true values.

Table 5.2 gives an overview of the R^2 scores calculated for the predictions belonging to the different models. The models implemented can be evaluated from the R^2score. The accuracy for Model 2 is slightly higher than the accuracy in Model 1 and Model 3, for pipe simulations 3 and 4. All three models has poor performance on pipe simulation 2. It is possible that the implementation of early stopping for model 1 and model 3 affects the training of the model. By stopping the algorithm before 30 epochs, the relationship between the variables may not have been fully detected. The results for each pipe will be discussed further in the following sections.

Table 5.2: R^2 score for the predictions

Pipe	Model 1	Model 2	Model 3
2	0.4874	0.4712	0.4037
3	0.9877	0.9907	0.9826
4	0.9580	0.9762	0.9683

5.6.2 Testing - Pipe 2

The first testing set was done on pipe 2, which has a larger diameter than the training set. The aim is to test the different models' abilities to predict pressure based on circumferential variation. For an increased diameter, the number of elements has increased. This

will affect the y-component of each normal, as there will be a smaller difference between each element.

From the R^2-score given in table 5.2, it is evident that the models does not provide a sufficient prediction for pipe 2. Figure 5.6(b) displays the relationship between the predicted values and the measured values for a randomly selected element. The element is placed at $Z = 9262mm$. The error is larger for the lower values of the pressure than for the high pressure values. Figure 5.6 displays the predictions for the same element. When plotting the prediction from the different models up against the simulated data obtained from the test set, some observations are made. Firstly, all the models have a higher starting pressure and a higher end pressure. Secondly, the simulated data only has one pressure decay, while the models predict two pressure decays. This might be due to the increased diameter, resulting in a higher crack speed. Because of the high crack speed, depressurization of CO_2 is not present, removing the first decay and saturation plateau. The models are not able to correctly predict the pressure decay from the crack. While the pressure decays towards 0 MPa, the predicted values all flatten around 4 MPa. A slight increase in the predictions is observed towards the end. This remains unexplained.

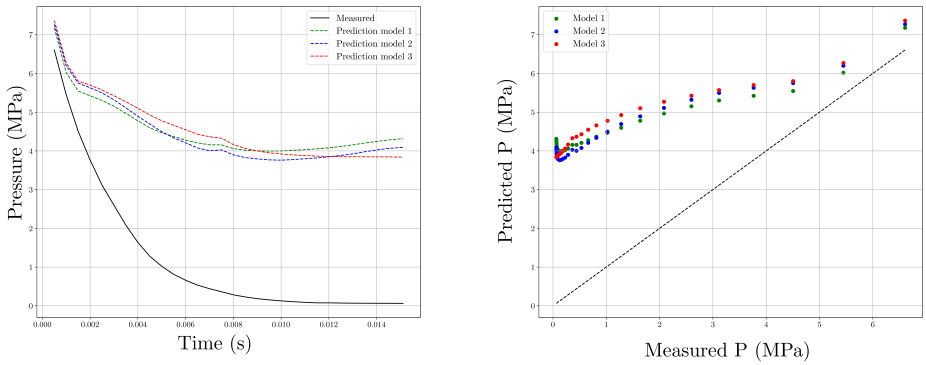

(a) (b)

Figure 5.6: Prediction for the different model for an element placed at $Z = 9262mm$

The predictions for pipe simulation 2 have been explored for multiple elements. For elements with a high Z position, the predictions will mostly estimate a higher pressure than what is measured. For elements with a low Z position, the curve for the measured data has been observed to be constant. This remains unexplained.

5.6.3 Testing - Pipe 3

Pipe 3 has been simulated with a lower diameter size than the simulation obtained for the training data. With a decreased diameter size, the number of elements along the circumference decreases accordingly. All models have a high R^2-score, with the second model being able to fit the measured data best. In figure 5.7 the predictions from the different models are plotted for a randomly selected element placed at $Z = 7375$ mm.

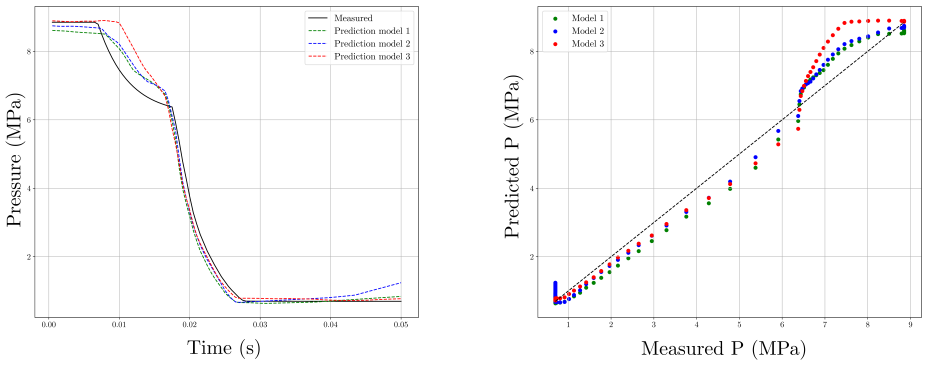

(a) (b)

Figure 5.7: Prediction for the different model for randomly selected element placed at $Z = 7375$ mm

From the plot, it is possible to see that all three models are able to predict a high start pressure and an end pressure close to the pressure obtained from the simulation. The initial pressure decay due to depressurization is predicted to be higher than the measured values indicates. Additionally, the plateau pressure is predicted to be about 0.5 MPa higher than the measured values. The pressure decay related to the crack opening has a good fit for all models. Although model 2 has the best R^2-score, an increase in the predicted pressure is seen towards the end of the simulation. It is possible that for this diameter and a longer propagating crack, the predictions would increase further. The predictions for pipe simulation 3 have been explored for several other elements. The predictions yield an overall good fit, and the predictions are mostly able to estimate a pressure close to the true values.

5.6.4 Testing - Pipe 4

The aim of test-set 4 is to check the models' capability to predict pressures when the running crack propagates for a longer axial distance than what the models have been trained on. In pipeline 4, the second pipe stoke has been assigned the same material and geometrical properties as the first pipe stoke. Still, the number of active elements is the same as the number of active elements in the training data. As the crack is propagating longer, the simulation time for the pipe is longer than the simulation time of the training data set. The calculated R^2-score of the models on the pipe indicates that the models have a good fit, with high accuracy. The predictions has been plotted up against the simulated values for a randomly selected element.

From figure 5.8, the measured pressure is plotted and its observed that the pressure only contains one decay, without the presence of the saturation plateau. The models accurately predicts the decay. However, all models predict a second decay, starting around 0.02 ms, and yield negative pressure beyond this time. It is believed that the models predict a

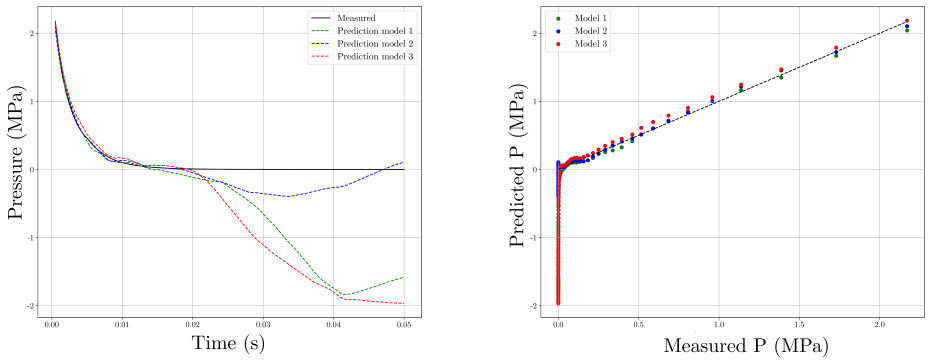

(a) (b)

Figure 5.8: Prediction for the different model for a randomly selected element

first decay as a result of decompression, and a second decay as a result of the crack propagation.

The predictions from the models are explored for several elements. The predictions have mostly a good fit. It is observed that the predicted pressure has the largest error toward the end of the time period, where crack arrest occur. Thus, the models might not have found the best representation for when the crack is allowed to propagate further.

5.7 Discussion

In the chapter, the machine learning models have been implemented and the results have been presented. From the results, it was observed that the developed models had varying results on the different test data. The developed models can, with high accuracy, predict the pressure decay in a pipe with a smaller diameter where the crack has been allowed to propagate for the same distance as in the training data. It is observed that when the crack is allowed propagate for a longer distance, the models will have inaccuracies. These inaccuracies are related to the simulation times where the crack has propagated further than what is observed in the training data. In order to create more accurate machine learning models, the training data should contain a broader range of cases. By including different pipe geometries in the training data, such as longer and shorter pipe stoke, the implemented models might be able to create better representations of the pressure during a running ductile fracture.

For the models to be applicable as surrogates in a simulation of running ductile fracture, the material properties should be accounted for as well. The data from the simulation all contain the same pipe material and thickness. The strength of the material and the wall thickness of the pipe will affect the speed of the propagating crack. Because of this, it can be beneficial to train machine learning models on data from different pipe steel alloys. If the data were to be trained for different materials and wall thickness, more reliable

results could be obtained from the machine learning models. Overall, the plotting of the predicted pressures indicates that the models yield a decent fit. The presented method can be further developed, and be an asset for the simulation of running ductile fractures.

Chapter 6

Concluding remarks

The main objective of this thesis was to train a neural network based on simulations of a running ductile fracture in pipelines transporting CO_2. This was achieved by studying the mechanisms of an RDF, as well as the pressure present in the pipeline. For the area behind the crack tip, spatial pressure decay has been observed experimentally. A reference pressure decay model was developed using experimental values, and the results from a validated coupled FSI model for pipeline simulation. The developed reference pressure decay model has taken the depressurisation of CO2 into account. The spatial pressure decay was calculated for two directions with regards to the crack, circumferential variation ξ and axial variation. The developed pressure decay model has a satisfactory fit when compared to existing pressure curves, and is believed to be describing the effects of CO_2 in a fractured pipeline. When plotting the developed models for an axial variation along the pipe, it was determined that the model was suitable for further use and application in simulations.

Further, the pressure model was applied as a load for a FE-simulation of pipelines. Four pipelines with different pipe geometries were simulated under the applied loading model developed. Three of the pipes had variations in pipe diameter. A fourth pipe was simulated containing equal pipe diameter as the first simulation, but without a pipe stoke acting as gas reservoir modelled. In the pipe simulations, all cracks propagated as expected, where three of the pipes arrested in the welds to the pipe stoke acting as gas reservoir. It was observed that the physical appearance of the crack was altered based on the pipe diameter. Further, it was observed that the crack speed was different for the varying pipe diameters. With higher pipe diameter, the pressure on the crack tip will become larger creating a faster crack speed. The physical properties of a running ductile fracture was present in all the simulations. The data obtained in the simulations was deemed as proficient for training and testing of a neural network.

Artificial neural network models were created and trained using the generated data from the first simulation of the pipelines. Three different artificial neural network architectures were implemented and trained. The loss of the models indicated that the networks had found a good representation, without overfitting. The predictive abilities of the implemented models were then tested on the simulations from the three remaining pipe geometries, and the accuracy of the predictions were calculated using R^2-score. For pipe

3 and pipe 4, the models showed great predictive capabilities, with high R^2-score. For pipe 2, where the diameter was increased, the R^2-scores were low, and all models were unable to accurately predict the pressure. This is believed to be due to the high crack speed in pipe 2, which will alter the pressure curves. In order to account for this, the neural network should be trained for several geometries. If this is done, it will be possible to use the training from the neural network as a surrogate pressure model in FEM-simulations of running fractures for efficient simulations. Additionally, for a surrogate model to truly become a suitable alternative, simulations should be made for several materials. The materials will have different strengths and the resisting force in the material could alter the speed of the propagating crack and the pressure inside the pipe. The training data could include material and geometry as variables in the training process as well, possibly increasing the predictive capabilities. The procedure and methodology proposed showed promising results with respect to predictive capability, and can be used as a surrogate model in engineering tools for simulating RDFs.

Future Work

Building upon the outcomes of this research, future improvements and examinations can be done for further developing the proposed methodology.

With the interest of creating a machine learning model able to quickly predict the pressure curves inside a pipe, the models should be re-applied into simulation tools. The neural networks should further be trained on more data, especially variations in geometry. Additionally, the training could include material data in further research.

The presented pressure decay model and simulations does not consider the effects of backfill. By incorporating backfill into the pressure decay models, the pressure inside the pipe could better describe the real-world pressure present in CCS pipelines at the seabed. This could improve the design further.

Further work could also generate the reference simulations using smoothed particle hydrodynamics techniques to represent the fluid within the pipeline. As immersed particle methods and smoothed particle hydrodynamics is beneficial for describing fluid through cracks, these simulations can provide better results for the simulation of the fluid-structure interaction.

References

[1] O. Edenhofer. *Climate change 2014: mitigation of climate change*, volume 3. Cambridge University Press, 2015.

[2] I. E. Agency. *Energy Technology Perspectives 2014*. 2014, page 380. DOI: https://doi.org/https://doi.org/10.1787/energy_tech-2014-en. URL: https://www.oecd-ilibrary.org/content/publication/energy_tech-2014-en.

[3] *Pipeline Fracture Control Concepts for Norwegian Offshore Carbon Capture and Storage*, volume Volume 3: Operations, Monitoring, and Maintenance; Materials and Joining of *International Pipeline Conference*, Sept. 2020. DOI: 10.1115/IPC2020-9766. URL: https://doi.org/10.1115/IPC2020-9766.

[4] Carbon capture and storage. en. URL: https://www.norskpetroleum.no/en/environment-and-technology/carbon-capture-and-storage/ (visited on 06/30/2023).

[5] E. Aursand, S. Dumoulin, M. Hammer, H. Lange, A. Morin, S. Munkejord, and H. Nordhagen. Fracture propagation control in co2 pipelines: validation of a coupled fluid–structure model. *Engineering Structures*, 123:192–212, 2016. ISSN: 0141-0296. DOI: https://doi.org/10.1016/j.engstruct.2016.05.012. URL: https://www.sciencedirect.com/science/article/pii/S0141029616302061.

[6] E. Aursand, C. Dørum, M. Hammer, A. Morin, S. Munkejord, and H. Nordhagen. Co2 pipeline integrity: comparison of a coupled fluid-structure model and uncoupled two-curve methods. *Energy Procedia*, 51:382–391, 2014. ISSN: 1876-6102. DOI: https://doi.org/10.1016/j.egypro.2014.07.045. URL: https://www.sciencedirect.com/science/article/pii/S1876610214009072. 7th Trondheim Conference on CO2 capture, Transport and Storage (2013).

[7] R. Higuchi, H. Makino, and I. Takeuchi. New concept and test method on running ductile fracture arrest for high pressure gas pipeline. In *24th world gas conference, WGC*, volume 4, pages 2730–2737, 2009.

[8] *Prediction of Rapid Ductile Crack Extension and Arrest by an Analytical Approach*, volume 2010 8th International Pipeline Conference, Volume 2 of *International Pipeline Conference*, Sept. 2010, pages 341–350. DOI: 10.1115/IPC2010-31176. URL: https://doi.org/10.1115/IPC2010-31176.

[9] *Analysis of Two Dense Phase Carbon Dioxide Full-Scale Fracture Propagation Tests*, volume Volume 3: Materials and Joining; Risk and Reliability of *International Pipeline Conference*, Sept. 2014. DOI: 10.1115/IPC2014-33080. eprint: https://asmedigitalcollection.asme.org/IPC/proceedings-pdf/IPC2014/46124/V003T07A003/4272279/v003t07a003-ipc2014-33080.pdf. URL: https://doi.org/10.1115/IPC2014-33080. V003T07A003.

[10] H. Mahgerefteh, S. Brown, and G. Denton. Modelling the impact of stream impurities on ductile fractures in co2 pipelines. *Chemical Engineering Science*, 74:200–210, 2012. ISSN: 0009-2509. DOI: https://doi.org/10.1016/j.ces.2012.02.037. URL: https://www.sciencedirect.com/science/article/pii/S0009250912001339.

[11] V. Keim, M. Paredes, A. Nonn, and S. Münstermann. Fsi-simulation of ductile fracture propagation and arrest in pipelines: comparison with existing data of full-scale burst tests. *International Journal of Pressure Vessels and Piping*, 182:104067, 2020. ISSN: 0308-0161. DOI: https://doi.org/10.1016/j.ijpvp.2020.104067. URL: https://www.sciencedirect.com/science/article/pii/S0308016120300454.

[12] *Fracture Control in Carbon Dioxide Pipelines: The Effect of Impurities*, volume 2008 7th International Pipeline Conference, Volume 3 of *International Pipeline Conference*, Sept. 2008, pages 229–240. DOI: 10.1115/IPC2008-64346. eprint: https://asmedigitalcollection.asme.org/IPC/proceedings-pdf/IPC2008/48593/229/4579296/229_1.pdf. URL: https://doi.org/10.1115/IPC2008-64346.

[13] I. Scheider, A. Nonn, A. Völling, A. Mondry, and C. Kalwa. A damage mechanics based evaluation of dynamic fracture resistance in gas pipelines. *Procedia Materials Science*, 3:1956–1964, 2014. ISSN: 2211-8128. DOI: https://doi.org/10.1016/j.mspro.2014.06.315. URL: https://www.sciencedirect.com/science/article/pii/S2211812814003162. 20th European Conference on Fracture.

[14] A new coupled fluid–structure modeling methodology for running ductile fracture. *Computers Structures*, 94-95:13–21, 2012. ISSN: 0045-7949. DOI: https://doi.org/10.1016/j.compstruc.2012.01.004. URL: https://www.sciencedirect.com/science/article/pii/S0045794912000053.

[15] S. Nasiri, M. R. Khosravani, and K. Weinberg. Fracture mechanics and mechanical fault detection by artificial intelligence methods: a review. *Engineering Failure Analysis*, 81:270–293, 2017. ISSN: 1350-6307. DOI: https://doi.org/10.1016/j.engfailanal.2017.07.011. URL: https://www.sciencedirect.com/science/article/pii/S1350630717301929.

[16] B. Paermentier, D. Debruyne, and R. Talemi. A machine learning based sensitivity analysis of the gtn damage parameters for dynamic fracture propagation in x70 pipeline steel. *International Journal of Fracture*, 227:111–132, 2021. ISSN: 1573-2673. DOI: https://doi.org/10.1007/s10704-020-00499-3.

[17] H. L. Burchardt and I. Saether. Modelling of Running Fracture in Steel Pipes for CO2 Transport, Trondheim, June 2022.

[18] *The Effects of Soil Properties on the Fracture Speeds of Propagating Axial Cracks in Line Pipe Steels*, volume Volume 3: Materials and Joining; Pipeline Automation and Measurement; Risk and Reliability, Parts A and B of *International Pipeline Conference*, Sept. 2006, pages 73–82. DOI: 10.1115/IPC2006-10086. eprint: https://asmedigitalcollection.asme.org/IPC/proceedings-pdf/IPC2006/42630/73/2654230/73_1.pdf. URL: https://doi.org/10.1115/IPC2006-10086.

[19] P. O'Donoghue, M. Kanninen, C. Leung, G. Demofonti, and S. Venzi. The development and validation of a dynamic fracture propagation model for gas transmission pipelines. *International Journal of Pressure Vessels and Piping*, 70(1):11–25, 1997. ISSN: 0308-0161. DOI: https://doi.org/10.1016/S0308-0161(96)00012-9. URL: https://www.sciencedirect.com/science/article/pii/S0308016196000129.

[20] G. Gruben and K. Macdonald. Advances in running ductile fracture assessment for the Longship full-scale CCS project, Lecture, Stavanger, Mar. 2023. URL: https://hdl.handle.net/11250/3061215.

[21] H. Makino and T. Amano. Demonstration of crack arrestability of x100 line pipe and development of evaluation technologies for three-dimensional fracture process. *Nippon steel & Sumitomo metal technical report*, (107), 2015.

[22] R. Talemi, S. Cooreman, H. Mahgerefteh, S. Martynov, and S. Brown. A fully coupled fluid-structure interaction simulation of three-dimensional dynamic ductile fracture in a steel pipeline. *Theoretical and Applied Fracture Mechanics*, 101:224–235, 2019. ISSN: 0167-8442. DOI: https://doi.org/10.1016/j.tafmec.2019.02.005. URL: https://www.sciencedirect.com/science/article/pii/S016784421830658X.

[23] J. Newman, M. James, and U. Zerbst. A review of the ctoa/ctod fracture criterion. *Engineering Fracture Mechanics*, 70(3):371–385, 2003. ISSN: 0013-7944. DOI: https://doi.org/10.1016/S0013-7944(02)00125-X. URL: https://www.sciencedirect.com/science/article/pii/S001379440200125X.

[24] A. L. Gurson. Continuum theory of ductile rupture by void nucleation and growth: part i—yield criteria and flow rules for porous ductile media. *Journal of Engineering Materials and Technology*, 99(1):2–15, 1977.

[25] V. Tvergaard and A. Needleman. Analysis of cup-cone fracture in a round tensile bar. *Acta Metallurgica*, 32(1):157–169, 1984.

[26] W. A. Maxey, J. F. Kiefner, and R. J. Eiber. Ductile fracture arrest in gas pipelines, Jan. 1976. URL: https://www.osti.gov/biblio/7014528.

[27] D.-J. Shim, G. Wilkowski, D. Rudland, B. Rothwell, and J. Merritt. Numerical simulation of dynamic ductile fracture propagation using cohesive zone modeling. In *International Pipeline Conference*, volume 48593, pages 21–28, 2008.

[28] A. Volling, M. Erdelen-Peppler, C. Kalwa, H. Brauer, B. Ouaissa, and H. Meuser. Numerical approach for crack-arrest prediction by fem. In *6th International Pipeline Technology Conference*, S19–01, 2013.

[29] G. Hou, J. Wang, and A. Layton. Numerical methods for fluid-structure interaction—a review. *Communications in Computational Physics*, 12(2):337–377, 2012.

[30] T. Rabczuk, R. Gracie, J.-H. Song, and T. Belytschko. Immersed particle method for fluid–structure interaction. *International Journal for Numerical Methods in Engineering*, 81(1):48–71, 2010.

[31] J. J. Monaghan. Smoothed particle hydrodynamics. *Annual review of astronomy and astrophysics*, 30(1):543–574, 1992.

[32] G. Demofonti, A. Maresca, and G. Buzzichelli. Ductile Fracture Propagation and Arrest in Offshore Pipelines. *Applied Mechanics Reviews*, 41(2):85–95, Feb. 1988. ISSN: 0003-6900. DOI: 10.1115/1.3151883. eprint: https://asmedigitalcollection.asme.org/appliedmechanicsreviews/article-pdf/41/2/85/5435462/85_1.pdf. URL: https://doi.org/10.1115/1.3151883.

[33] E. Aursand, P. Aursand, T. Berstad, C. Dørum, M. Hammer, S. T. Munkejord, and H. O. Nordhagen. Co2 pipeline integrity: a coupled fluid-structure model using a reference equation of state for co2. *Energy Procedia*, 37:3113–3122, 2013.

[34] H. Makino, T. Inoue, S. Endo, T. Kubo, and T. Matsumoto. Simulation method for shear fracture propagation in natural gas transmission pipelines. *International Journal of Offshore and Polar Engineering*, 14(01), 2004.

[35] V. Keim, A. Nonn, and S. Münstermann. Application of the modified bai-wierzbicki model for the prediction of ductile fracture in pipelines. *International Journal of Pressure Vessels and Piping*, 171:104–116, 2019.

[36] G. Berardo, P. Salvini, G. Mannucci, and G. Demofonti. On longitudinal propagation of a ductile fracture in a buried gas pipeline: numerical and experimental analysis. In *International Pipeline Conference*, volume 40245, V001T02A025. American Society of Mechanical Engineers, 2000.

[37] L. Xue, V. Keim, M. Paredes, A. Nonn, and T. Wierzbicki. Anisotropic effects on crack propagation in pressurized line pipes under running ductile fracture scenarios. *Engineering Fracture Mechanics*, 249:107748, 2021. ISSN: 0013-7944. DOI: https://doi.org/10.1016/j.engfracmech.2021.107748. URL: https://www.sciencedirect.com/science/article/pii/S001379442100196X.

[38] J. O. Hallquist et al. Ls-dyna keyword user's manual. *Livermore Software Technology Corporation*, 970:299–800, 2007.

[39] R. Span and W. Wagner. A new equation of state for carbon dioxide covering the fluid region from the triple-point temperature to 1100 k at pressures up to 800 mpa. *Journal of physical and chemical reference data*, 25(6):1509–1596, 1996.

[40] *Abaqus/CAE - SIMULIA User Assistance 2022*. 1978 - 2022 Dassault Systemes Simulia Corp. URL: https://help.3ds.com/2022/English/DSSIMULIA_Established/SIMULIA_Established_FrontmatterMap/sim-r-DSDocAbaqus.htm?contextscope=all&id=ec01bc8c83d743a6a30123c5a034edca.

[41] I. Goodfellow, Y. Bengio, and A. Courville. *Deep Learning*. MIT Press, 2016. http://www.deeplearningbook.org.

[42] M. A. Nielsen. *Neural Networks and Deep Learning*. Determination Press, 2015.

[43] Y. LeCun, Y. Bengio, G. Hinton, et al. Deep learning. nature, 521 (7553), 436-444. *Google Scholar Google Scholar Cross Ref Cross Ref*:25, 2015.

[44] D. Freedman, R. Pisani, and R. Purves. Statistics (international student edition). *Pisani, R. Purves, 4th edn. WW Norton & Company, New York*, 2007.

[45] Martín Abadi, Ashish Agarwal, Paul Barham, Eugene Brevdo, Zhifeng Chen, Craig Citro, Greg S. Corrado, Andy Davis, Jeffrey Dean, Matthieu Devin, Sanjay Ghemawat, Ian Goodfellow, Andrew Harp, Geoffrey Irving, Michael Isard, Y. Jia, Rafal Jozefowicz, Lukasz Kaiser, Manjunath Kudlur, Josh Levenberg, Dandelion Mané, Rajat Monga, Sherry Moore, Derek Murray, Chris Olah, Mike Schuster, Jonathon Shlens, Benoit Steiner, Ilya Sutskever, Kunal Talwar, Paul Tucker, Vincent Vanhoucke, Vijay Vasudevan, Fernanda Viégas, Oriol Vinyals, Pete Warden, Martin Wattenberg, Martin Wicke, Yuan Yu, and Xiaoqiang Zheng. TensorFlow: large-scale machine learning on heterogeneous systems, 2015. URL: https://www.tensorflow.org/. Software available from tensorflow.org.

[46] F. Chollet et al. Keras. https://keras.io, 2015.

Appendices

A - Pipe simulations

A1 - Pipe simulation 1

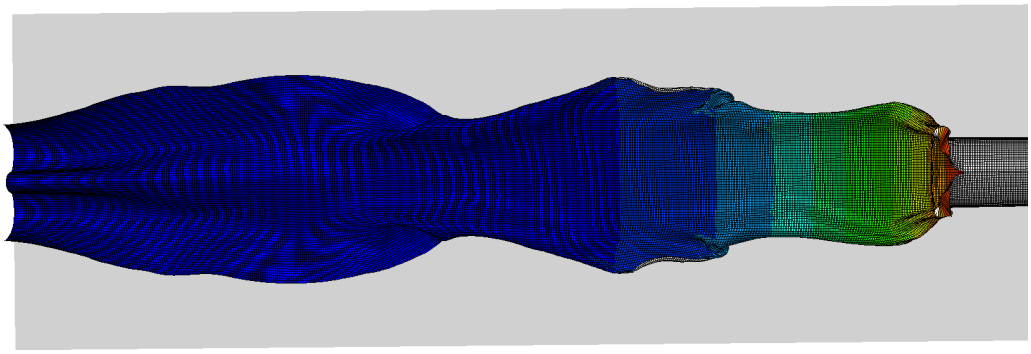

Figure A.1: Pipe 1 seen from above

A2 - Pipe simulation 2

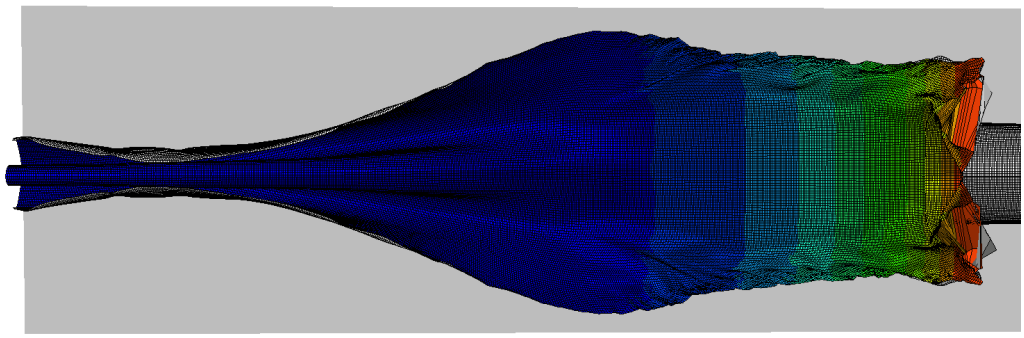

Figure A.2: Pipe 2 seen from above

A3 - Pipe simulation 3

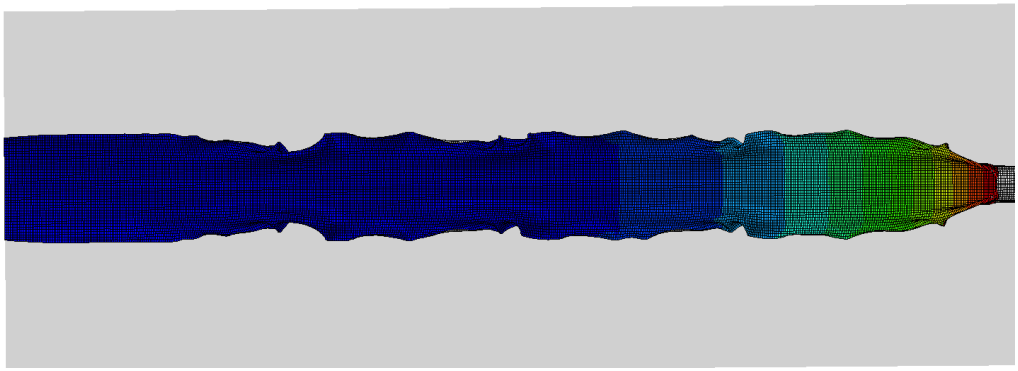

Figure A.3: Pipe 3 seen from above

A4 - Pipe simulation 4

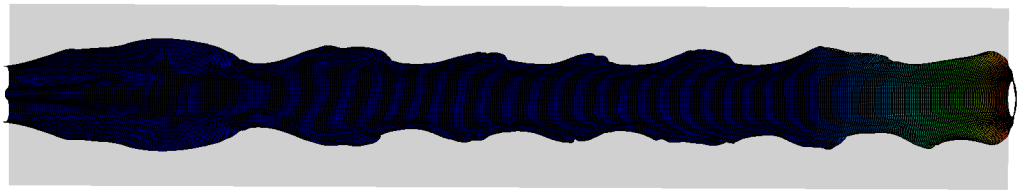

Figure A.4: Pipe 4 seen from above

B - Testing data

B1 - Variable range pipe 2

Table B.1: Range for the variables for pipe 2

Parameter	min	max
t (s)	0.0005	0.015
Z_c (mm)	8706	8928
Z (mm)	−32313	15969
N	−0.999	1.000
P (MPa)	0.0004	8.850

B2 - Variable range pipe 3

Table B.2: Value range for the variables of pipe 3

Parameter	min	max
t (s)	0.0005	0.050
Z_c (mm)	5509	10314
Z (mm)	4.898	10995
N	−0.999	1.000
P (MPa)	0.009	8.850

B3 - Variable range pipe 4

Table B.3: Value range for the variables of pipe 4

Parameter	min	max
t (s)	$5.004 \cdot 10^{-4}$	$5.000 \cdot 10^{-2}$
Z_c (mm)	5.531	9627
Z (mm)	-114.2	10995
N	-1.000	1.000
P (MPa)	0.00001	8.850

C - Heat-maps

C1 - Heat-map pipe data 2

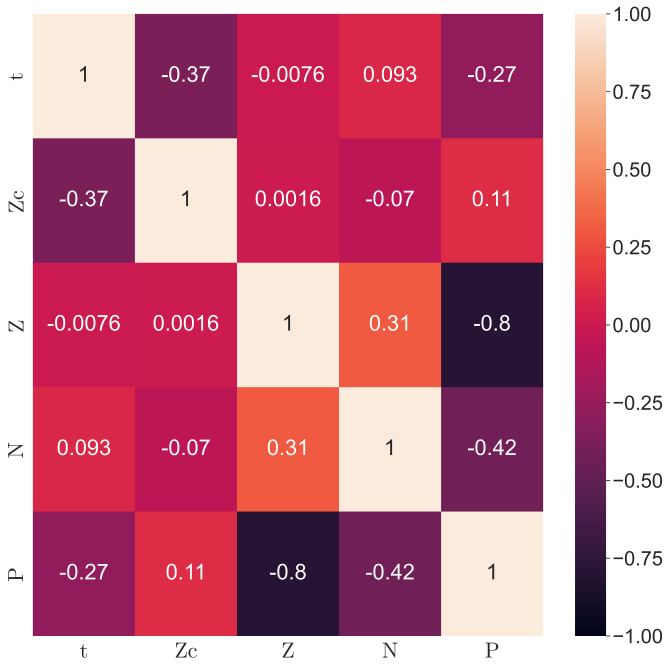

Figure C.1: Correlation matrix for data from pipe simulation 3

C2 - Heat-map for pipe data 3

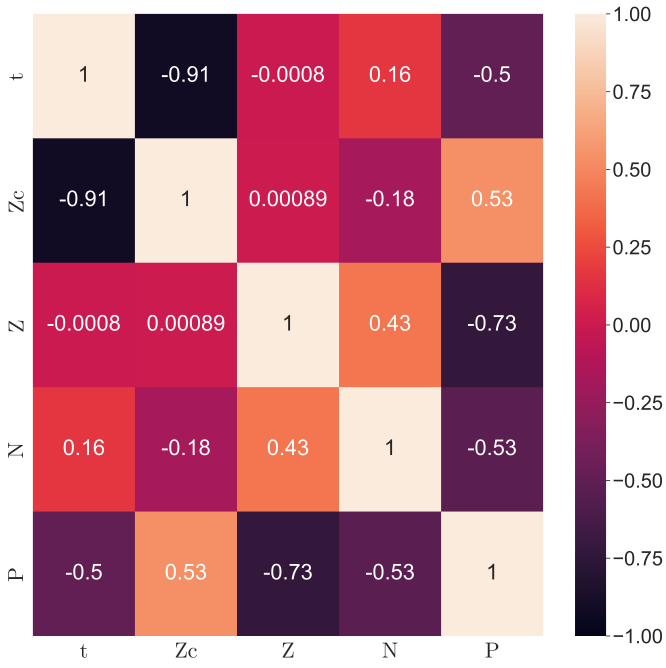

Figure C.2: Correlation matrix for data from pipe simulation 3

C3 - Heat-map for pipe data 4

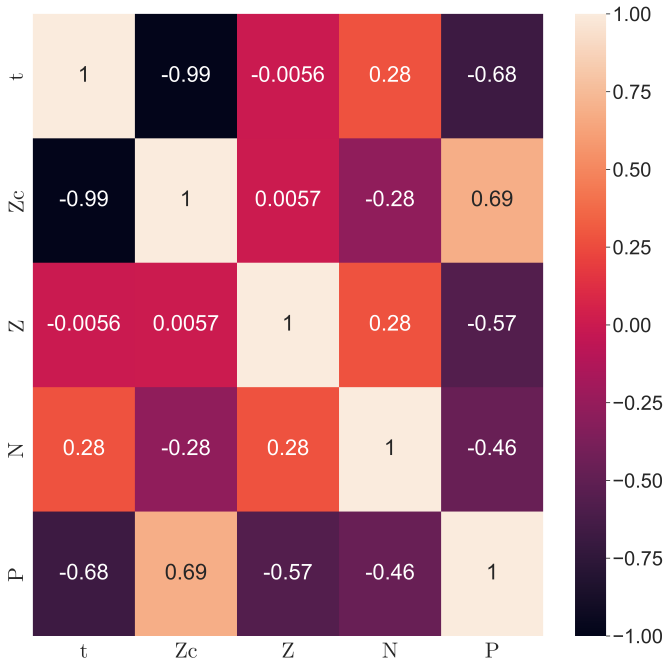

Figure C.3: Caption

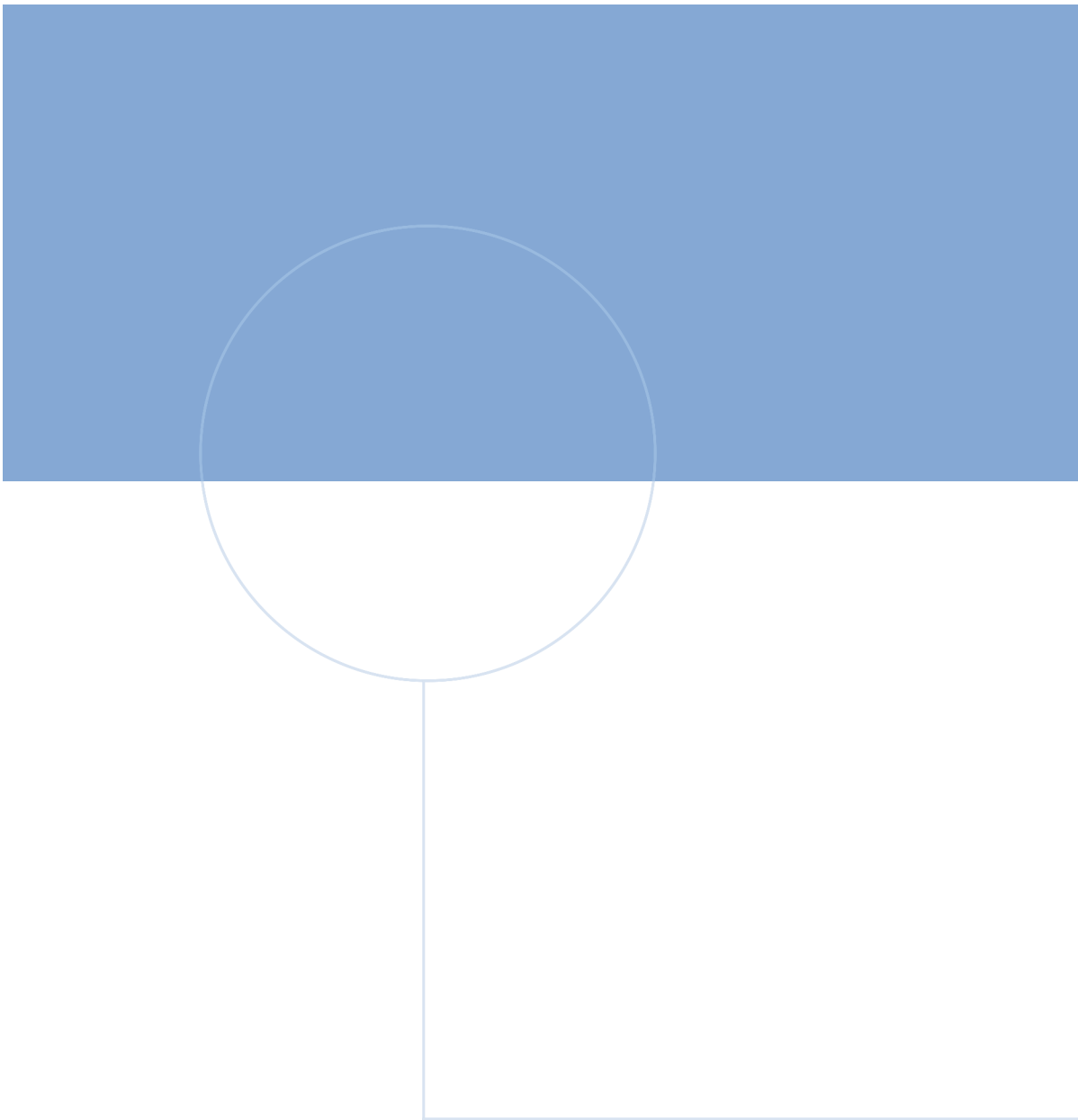

NTNU

Kunnskap for en bedre verden